Empowering Clean Water whilst Safeguarding Water Distribution Pipeline Integrity: Towards Manganese- and Iron-Free Lime Hydrate for Water Treatment

Dávid Kocsis,[*1,2,3] Rhys A. Ward,[2,3] Christopher R. Meyer,[*1]
Michael Thompson,[4] Timothy J. Prior,[4] Stephen M. Kelly,[3,4]
Nathan S. Lawrence,[2,3] Jay D. Wadhawan[*2,3]

[1]*Singleton Birch, Ltd., Melton Ross Quarries,*
Barnetby DN38 6AE, North Lincolnshire, United Kingdom.

[2]*Department of Chemical Engineering, The University of Hull,*
Cottingham Road, Kingston-upon-Hull HU6 7RX, United Kingdom.

[3]*Aura Innovation Centre, Bridgehead Business Park,*
Meadow Road, Hessle HU13 0GD, United Kingdom.

[4]*Department of Chemistry, The University of Hull,*
Cottingham Road, Kingston-upon-Hull HU6 7RX, United Kingdom.

To be submitted to *Environ. Sci.: Water Res. Technol.*

[*]Corresponding authors:
E.mail: dkocsis@singletonbirch.co.uk (DK); cmeyer@singletonbirch.co.uk (CRM); j.wadhawan@hull.ac.uk (JDW)

Graphical Abstract

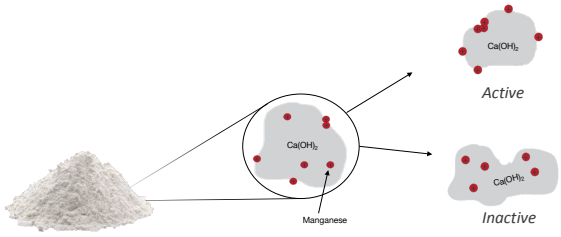

Active and passive manganese and iron impurities in drinking water-grade lime hydrate are removed through redox treatment.

Water Impact Statement

Reducing the amount of manganese and iron impurities present in drinking water treatment chemicals can improve both the æsthetic water quality and the integrity of its distribution pipelines, as it reduces the occurrence of discoloured water and pipescale. Herein, we develop treatments to remove these species from lime hydrate manufactured for the water industry, and provide "rules-of-thumb" for their scale-up.

Abstract

Hydrated limes are amongst the most economically valuable alkalis used by the water industry for the treatment of potable water. They are typically manufactured from the thermal decomposition of high purity limestones. However, the latter contain both manganese and iron impurities, which are transformed into the oxides Mn_3O_4 and Fe_2O_3 on burning in kilns (between 900 – 1100 ^{o}C) during the manufacture of lime, and are retained in the lime hydrate upon slaking. These impurities can be released through oxidation by conventional water disinfection chemicals (such as alkaline hypochlorite) during the use of lime hydrate as the alkaline pH modifier during conventional operations in water treatment works. This work investigates the redox mechanisms for manganese and iron removal from lime hydrate using alkaline hypochlorite: for manganese, interfacial electron transfer occurs first leading to dissolution as permanganate; in the case of iron impurities, solubility is encouraged in oxygenated solutions first through formation of solid ferrite, with oxidative dissolution of ferrite to ferrate. As expected for activation-controlled reactions, the oxidative dissolution is enhanced with increased temperatures; mapping the dissolution process with time allows for the unravelling of "rule-of-thumb" relationships for impurity removal of ~1%/min for manganese and ~3%/min for iron at 90 ^{o}C in alkaline hypochlorite.

Key words: Water treatment, manganese and iron impurities, lime, permanganate, ferrate, surface kinetics, dissolution, activation controlled reaction, climate-smart impurity removal

Introduction

Although *access* to safe drinking water is a mandated human right,[1] clean water *distribution* has been plagued by pipeline integrity issues, even in high-income countries, for at least the last 90 years.[2] In England, drinking water, supplied by water companies and authorities, is subjected to economic, environmental and public health regulation, by the Water Services Regulation Authority (Ofwat), the Environment Agency, and the Drinking Water Inspectorate (DWI), respectively.[3] Drinking water *quality* is governed by compliance with legislative standards (such as the European Drinking Water Directive 98/83/EC), which are based on guidelines published by the World Health Organisation.[4] These standards set upper limits on the presence of a wide range of ions and compounds, predominantly based on their toxicity; potable water is frequently contaminated by both natural effects (associated with groundwater/reservoir hydrology and biology),[5] and anthropogenic causes.[6] These impurities can be removed in water treatment works through the addition of chemical coagulants (such as alum and ferric sulphate) followed by clarification and filtration, with a subsequent disinfection step using, amongst others, chlorine or ozone, to remove micro-organisms.[7] There is an additional consequence for drinking water treatment that results from the historical use of lead piping infrastructure in its distribution: the corrosion of this material is a public health hazard (most infamously demonstrated through the 2014-19 Flint Water Crisis);[8] plumbosolvency control in the water mains relies on tiny solubility products, necessitating the addition of phosphates during water treatment, so as to maintain an extremely low concentration of soluble lead ions.

Manganese and iron are two essential mineral elements which are, likewise, regulated as a result of both toxicity (as Mn^{2+}), and their propensity (as black and red oxides) to cause pipe-scale[4,9] – the lining of the water distribution pipelines, causing restricted flow, and ultimately requiring more energy to be expended so as to deliver water to consumers than in an de-scaled pipeline. Although iron in drinking water is generally present at sufficiently low concentrations so as not to present a health hazard (there is no toxicity-based limit on iron in drinking water), manganese in drinking water may have adverse effects on intellectual and cognitive development, causing it to have an upper guideline value of 400 ppb.[4,9] Nevertheless, the guidelines recommend upper thresholds on manganese (50 ppb) and iron (200 ppb), to reduce “metallic taste” and prevent so-called “black water” and “red water” phenomena, respectively.[4,9] In the UK, these two discoloured water types are often a source of customer contacts (complaints) with water companies and authorities: in 2020, 1.8 M consumers (up from 1.1 M in 2019) were affected by the supply of tap water with an unæsthetic appearance (colour, taste and odour), as catalogued in Chief Inspector’s Report from the DWI,[10] with the largest number of complaints stemming from North-West England, the Midlands and Wales – areas where the water supply is fed by upland surface waters.[10,11] Such contacts cause the water companies and authorities to be fined by Ofwat. These problems with drinking water *distribution*, arise from a variety of factors, such as the increase

in water use due to hot weather,[10,11] the inadequate treatment of raw waters,[11,12] or during the improvement of the energy efficiency of water distribution by dislodging manganese- and iron-based oxide debris and pipe-scale using increased hydraulic pressure.[9,11,12] Since the solubility of manganese and iron oxides is both redox- and pH-sensitive, control of manganese and iron in the water supply is achieved through (1) understanding reservoir geology and water hydrology,[11] (2) designing water treatment works to incorporate elaborate filtration operations[13] which may be gravel-based, or involve "greensand" (glauconite, $(K,Na)(Fe^{III},Al,Mg)_2(Si,Al)_4O_{10}(OH)_2$, coated with manganese dioxide), and (3) reducing the amount of manganese-oxidising bacterial biofilms,[9,12a,14] *via* efficient disinfection of the water supply.[9,15,16]

It is also important to control the impurity level present in the *chemicals used to treat drinking water*: the volume of chemicals used in water treatment mean that even small reductions can provide benefit. Alkalis (pH modifiers) represent one of the largest group (by volume) of chemicals used by the UK water industry (in excess of 70 kTe/yr),[17] with a slight favouring (53%) of slaked lime (portlandite, lime hydrate, $Ca(OH)_2$) over caustic soda (NaOH).[17a] Lime is unusual in that it can be used both to remove manganese from reservoir water,[2,18a,b] and, as observed in KwaZulu-Natal, South Africa, brown lime (added during the treatment process) can be a source of manganese, even when the raw water has appreciable amounts of manganese.[18c] Lime softening of water through impurity removal is thought to occur *via* carbonation of portlandite,[19a] followed by heavy metal removal through sorption.[19a,b] Removal of impurities containing silicon and phosphorous, can be achieved through their reactive addition to lime or hydrate.[19c] In the UK, water-grade alkalis currently conform to European Standard CEN TC 164/WG9/TG5, with purity criteria for both caustic (BS EN 896) and lime (BS EN 12518) regulating the concentrations of fluorides, radionuclides and heavy metals (arsenic, cadmium, chromium, mercury, nickel, lead, antimony and selenium), with further limits imposed on lime for SiO_2, Al_2O_3, Fe_2O_3, MnO_2 and $CaCO_3$ impurities.[17a] This mandates the use of lime derived from *industrial grade limestones* only for water treatment. Such limestones are often referred to as pure carbonates (>95 wt.% combined $CaCO_3$ and $MgCO_3$), which are readily available across the globe: Figure 1a depicts the distribution of the total area (4.1 million km^2) of pure carbonate outcrops in the world,[20] with the distribution of the manufacture of 420 MTe/yr of lime (the average global production rate in 2016-2020)[21a] presented in Figure 1b. Using the data for the UK as an example, it is clear that *ca.* 2 wt.% of all lime production is required for water treatment purposes,[21b] so that the global requirement of lime hydrate is *ca.* 11 MTe/yr – a quantity that is not economically viable to manufacture without calcination of limestone.

The British Geological Survey have mapped the areas where pure calcium carbonate outcrops occur in England and Wales (see Table 1);[22] current UK lime manufacturing[23] is derived from either the high, or very high, purity limestones found in North Lincolnshire

(a)

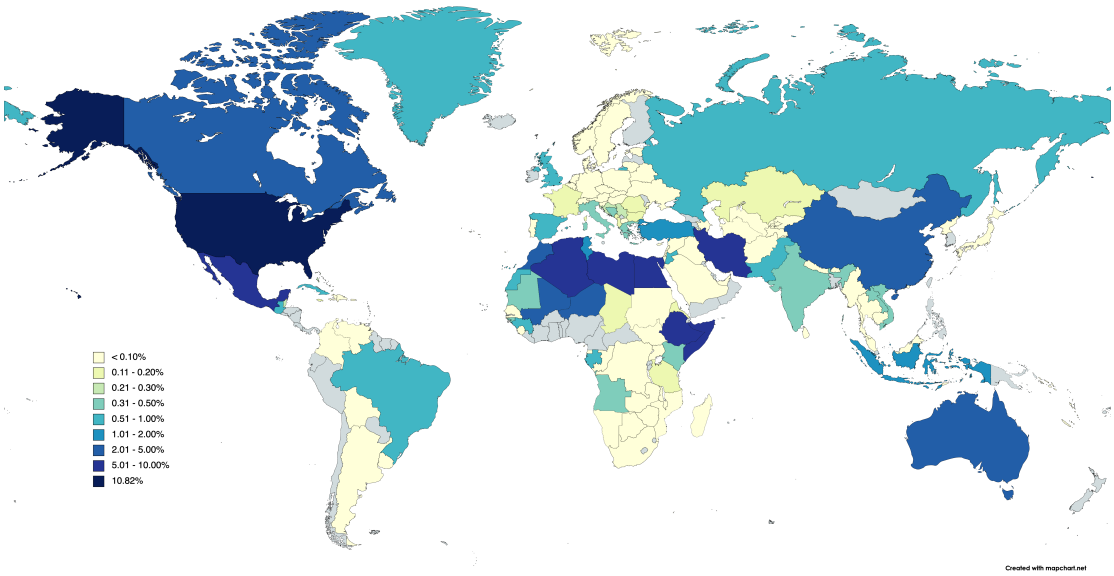

(b)

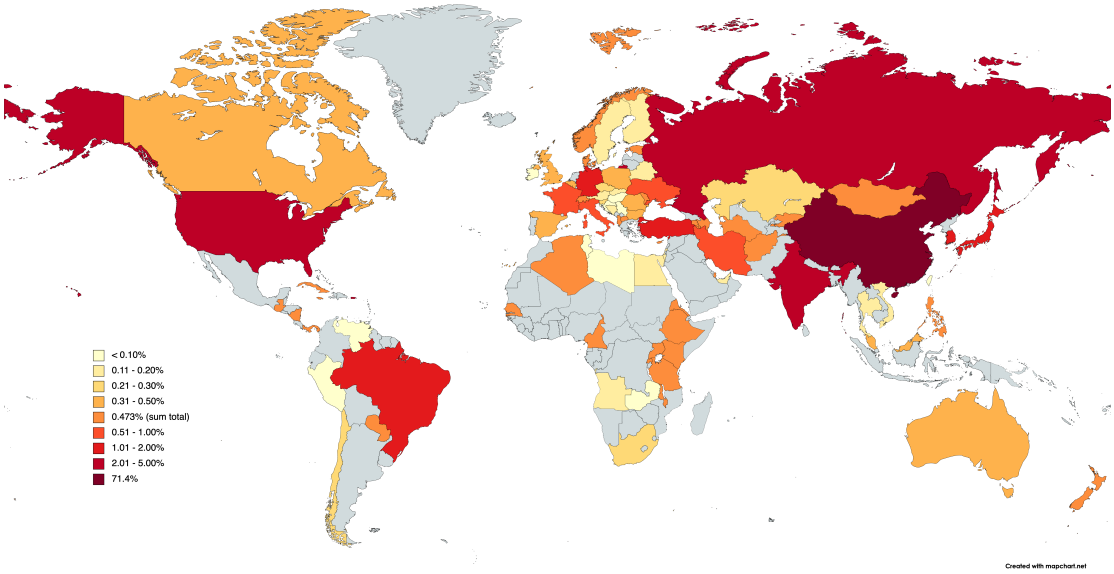

Figure 1: *World distribution maps illustrating the country breakdown of (a) pure carbonate rock outcrops, and (b) lime production. In both cases, data are expressed as a percentage of the world totals: (a) 4.1 million km^2 and (b) 420 MTe/yr (average for 2016-2022), with the country with the greatest pure carbonate rock outcrop area (USA) or the highest lime production (Republic of China) indicated separately. Note that in (b), only the sum total of the individual countries is given with the colour corresponding to 0.473%, and that other nations (in grey) may have produced lime over the 2016-2020 period. Data taken from (a) reference 20, and (b) reference 21, with both maps being drawn using software available at MapChart.Net.*

(Welton Formation of Cretaceous Chalk)[24] or the Derbyshire Dome (Bee Woo Formation of Carboniferous Limestones).[25] However, although these are all >97 wt.% $CaCO_3$, they are typically not "manganese-free", and therefore may introduce manganese into the drinking water distribution network, unless first cleaned to remove the manganese impurities.

In this paper, we illustrate redox chemical processes to treat water-grade lime derived from both high purity and very high purity limestones, so as to reduce the extent of manganese and iron impurities that they contain. We use insights into the physicochemical dynamics underpinning the impurity removal process to develop important design relationships for suitable process operations that could be integrated within existing lime manufacturing plants. We first provide an overview of the distribution of these impurities in both Carboniferous Limestone and Cretaceous Chalk (see Electronic Supplementary Information, ESI1), and indicate how these change during the lime cycle for the production of slaked lime.

Table 1: *Typical iron and manganese impurity levels in industrial grade limestones in England and Wales.*[†,‡]

Location	Formation	CaO /wt.%	Fe_2O_3 /wt.%	MnO /wt.%
Carboniferous Limestone				
Peak District	Bee Low	55.41	0.07	0.02
Mendips	Burrington Oolite	55.24	0.01	0.00
South Wales	Oxwich Head	55.80	0.02	0.01
North Wales	Llandulas	55.38	0.10	0.15
North Pennines	Cove	55.73	0.01	0.01
Lake District	Park	55.52	0.03	0.05
Average (Carboniferous Limestone)		***55.51***	***0.04***	***0.04***
Standard Deviation		***0.21***	***0.04***	***0.06***
Cretaceous Chalk				
Humberside	Welton	54.81	0.04	0.05
Humberside	Flamborough	53.60	0.10	0.06
Wiltshire	Upper Chalk	54.87	0.06	0.15
Wiltshire	Upper Chalk	54.93	0.03	0.03
Kent	Upper Chalk	55.45	0.04	0.04
Suffolk	Upper Chalk	54.94	0.08	0.06
Average (Cretaceous Chalk)		***54.77***	***0.06***	***0.07***
Standard Deviation		***0.62***	***0.03***	***0.04***

[†] *Adapted from data provided as Tables 3 and 12 in reference 22c.*
[‡] *Very high purity limestone is >98.5 wt.% $CaCO_3$, corresponding to >55.2 wt.% CaO; high purity limestone has $CaCO_3$ in the range 97-98.5 wt.%, corresponding to CaO in the range 54.3 – 55.2 wt.%, using conventional assessment criteria – see Table 5 of reference 26a. Note that the Flamborourgh Chalk Formation is technically of medium purity.*

Manganese and Iron Impurities in High Purity Limestones

The British Geological Survey describes limestones as being high purity, or very high purity depending on whether the mass fraction of $CaCO_3$ present therein is between 97.0% and 98.5%, or above 98.5%, respectively.[26] These are the only two categories of limestone considered to be suitable as industrial grade for use in the water treatment, iron and steel, chemicals, glass making, filters and pigments, paper and flue gas desulphurization industries.[22,27] Table 1 illustrates the typical compositional variation of both manganese (as MnO) and iron (as Fe_2O_3) impurities within high and very high purity limestone (limestone and chalk) strata in England and Wales.[22c] It is clear that, with the exception of the Burlington Oolite, ***all*** high purity (Cretaceous) and very high purity (Carboniferous) limestones in Table 1 are contaminated by both iron and manganese, with the slightly lower purity chalk being more uniform in its impurity distribution – the relative standard deviations are high for Carboniferous Limestones (92% (Fe) and 141% (Mn)), but much lower for the Cretaceous Chalk (47% (Fe) and 67% (Mn)), across all locations. This general picture is slightly misleading, since different parts of a limestone quarry can expose different depths of the limestone stratigraphy – for example, the Hindlow Quarry (Carboniferous Limestone from the Peak District) is reported to have manganese levels between 80-160 ppm, and iron levels between 200-500 ppm;[25] in contrast the Tunstead Quarry (Carboniferous Limestone from the Peak District) has manganese levels in the range 80-960 ppm, with iron levels ranging between 200-3000 ppm.[25] It appears that small variations in the rock lithology can lead to a wide variation in the level of the iron and manganese contaminants:[22,26] such local variations can downgrade the purity of limestones,[22,26] and, since limestones (including hard Northern Province Chalk – see Electronic Supplementary Information, ESI1) are typically blasted from a rock face, it is not always possible to separate out these impurities.[27]

Manganese and iron impurities in limestones derive from a number of sources, such as the iron sulphides (pyrite and marcasite) present in clay bands (wayboards), through dolomitization (minerals such as ankerite and kutnohorite), or through "accessory" minerals including tourmaline, garnet, magnetite, rhodochrosite and siderite.[22,24,25,28] Since limestones are permeable, it is thought that incongruent reactions at the particle surfaces release Mn^{2+} and Fe^{2+} ions into either recharge or connate water, resulting in a purer calcite.[28] Thus, under oxidising conditions (E_h > *ca.* 300 mV, see Electronic Supplementary Information, ESI2), manganese and iron can be deposited as dendrites at shallow fracture surfaces as the oxides (such as pyrolusite, MnO_2), sesquioxides (braunite, Mn_2O_3, bixbyite, and hæmatite, Fe_2O_3), oxohydroxides (for example, manganite, MnOOH, and gœthite, α-FeOOH), hydroxides and hydrated iron oxides (including limonite).[29-32] Typically iron and manganese oxides in limestones occur in separate deposits. However, where they occur together, the iron oxides typically overlay the older manganese oxide deposits,[29] indicating that the manganese oxides enable the precipitation of iron oxides.[33] Under reducing conditions, the divalent impurities

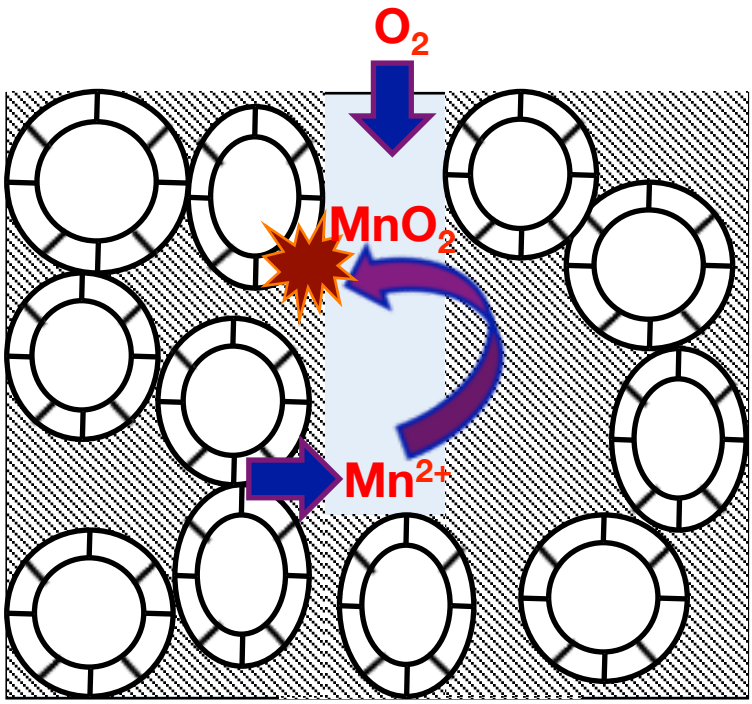

Figure 2: *Schematic illustration of dissolution/re-precipitation reactions causing the mineralisation of manganese (as radial dendritic growths) through incongruent reactions at fracture surfaces in the presence of interstitial or connate or recharge water. Adapted from reference 28.*

can be incorporated as interstitial solid solutions in the calcite (or, in the case of Limestone, calcite and aragonite) particles.[29,34] Such solution/re-deposition chemical processes (see Figure 2) are characteristic origins of manganese ores,[29] including the famous deposits at Nikopol (Ukraine) and Chiaturi (in the Caucasus).[35]

Manganese and Iron Impurities in Slaked Limes

The manufacture of lime hydrate first involves the comminution of limestones, followed by the stages of calcination and then reaction with water (see Electronic Supplementary Information, ESI3).[27] During the calcination process to form quicklime (CaO, molar mass 56 g/mol), carbon dioxide is lost from the calcite ($CaCO_3$, molar mass 100 g/mol), so that although there is a small degree of shrinkage of the rock,[27] the concentration of solid impurities increases. Singleton Birch, Ltd.'s high calcium quicklime, Burnt Lime 40,[36] although hard to quantify exactly owing to its high reactivity with atmospheric moisture and carbon dioxide, typically comprises >90 wt.% CaO, with small degrees of impurities derived from both the limestone rock and the sulphur from the natural gas used in the calcination. Digestive analysis (see Electronic Supplementary Information, ESI4) of quicklime indicates a doubling of the manganese and iron concentration in lime compared with chalk (Figure 3). No differences were found between the size fractions investigated (~50 mm for Burnt Lime 40, or 3.35 mm finer screenings). The slight difference between the ratios for manganese and iron in lime *versus* the quarried rock, is indicative of the fact that both impurities derived from different oxidation forms in the chalk: the mass loss is consistent with Fe_2O_3 (Fe^{III}) and Mn_3O_4 (hausmannite, where (Jahn-Teller distorted) Mn^{III} occupies all of the octahedral sites, with Mn^{II} distributed in the tetrahedral sites in a cubic oxide lattice) being the impurities in quicklime, and Mn_2O_3 and either $FeCO_3$ or FeS_2 as the impurities in the chalk. This interpretation is consistent with the reported thermodynamic stability of manganese and iron oxides, carbonates and disulphides at kiln temperatures (900 – 1100 ^{o}C).[37,38] Note that whilst the kiln temperature is controlled to avoid sintering ("dead-burned lime"), the maximum upper temperature is close to that for the tetragonal-to-cubic phase change of the hausmannite spinel (1170 ^{o}C).[39]

Slaked lime is manufactured through reacting quicklime with a slight excess of the stoichiometric amount of water, to afford lime hydrate ($Ca(OH)_2$). The exothermicity of this reaction (temperatures can reach up to 150 ^{o}C) causes the excess water to vaporise, so that the impurities will remain in the solid state. The lime hydrate is a fine white powder, with an average particle diameter of 5 μm, and is a porous material of extremely high specific surface area (>20 m^2/g).[36] As indicated in Figure 3, on slaking the lime, the mass increase in going from CaO to $Ca(OH)_2$ (molar mass 74 g/mol) causes the impurity concentration to decrease by similar amounts for manganese and iron impurities. This suggests that the chemical nature of the manganese impurity is essentially unaffected by slaking, even if the iron

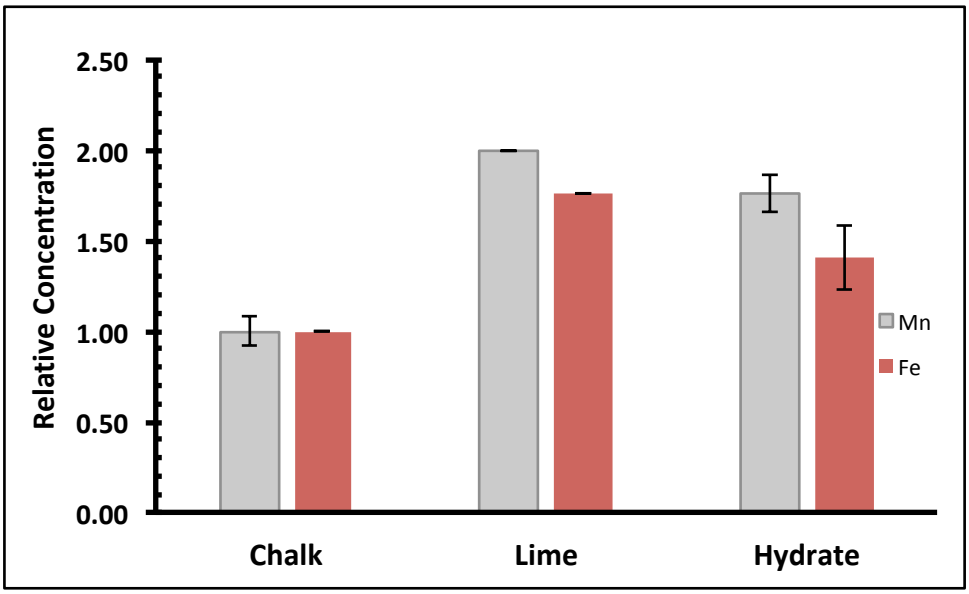

Figure 3: *Manganese and iron impurities within the lime cycle (Chalk is $CaCO_3$; lime refers to CaO; hydrate refers to $Ca(OH)_2$). Data obtained through HF digestion of the sample, followed by ICP-OES analysis (see Electronic Supplementary Information, ESI4). Note that in these plots, manganese (grey) and iron (red) levels, recorded as ppm (mg/kg), have been normalised to the average manganese or iron level present in quarried chalk. Error bars indicate one standard deviation over at least three samples.*

contaminants form hydrated oxides. As indicated in Electronic Supplementary Information, ESI5, slaked lime manufactured by Singleton Birch, Ltd. is typically *ca.* 97 wt.% portlandite ($Ca(OH)_2$). Accordingly, we may envisage that the particles of lime hydrate can be considered as existing with both "hard" core of $CaCO_3$ surrounded by a "softer", porous shell of $Ca(OH)_2$. This visualisation is a little primitive, since re-carbonation of the surface of the intermediate lime particles can take place. Nevertheless, in terms of impurity distribution and dispersion, we consider the following: Fe_2O_3 (core/shell), $FeS_2/FeCO_3$, (core), Mn_2O_3 (core) and Mn_3O_4 (core/shell).

The manganese and iron impurities in lime hydrate cannot be removed by water alone, as will be discussed later. It follows that a solution-based chemical etching process is necessary to remove iron and manganese impurities from lime hydrate. However, as the hydrate buffers the solution at very high pH (*ca.* 12.3), an etching process involving reduction of the impurities to the soluble divalent ions is flawed, as this will cause the impurities to be precipitated as the (coloured) hydroxides onto the white hydrate.[40] Accordingly, we consider the oxidative etching of the impurities.

Oxidative Removal of Manganese and Iron Impurities from Slaked Lime

In preliminary experiments, 1 g of slaked lime were incubated overnight with 100 g (80 mL) of of alkaline hypochlorite solution (~8%, density ~1.25 g/mL) and left, without stirring, in an open beaker at ambient temperature, after which a pale pink supernatant was observed. Spectroscopic analysis (see Electronic Supplementary Information, ESI6) afforded both a split-peak at *ca.* 520 nm, corresponding to the permanganate (MnO_4^-) anion, and a peak at 505 nm, which matches-up with that expected from ferrate (FeO_4^{2-}).[41] (Indeed, when the inverse spinel magnetite, Fe_3O_4, was treated under similar conditions, a purple supernatant, corresponding to ferrate was observed.) These experiments were repeated using slaked lime manufactured from rocks derived from throughout the Welton Formation of the Cretaceous Chalk at the Melton Ross Quarry ((North Lincolnshire, UK), in addition to slaked lime derived from Bee Low Carboniferous Limestone (Derbyshire, UK), both in the presence and absence of oxygen. In these experiments, after soaking the slaked lime in alkaline hypochlorite for a variable, fixed time periods, the pink supernatant was removed through vacuum filtration, and owing to the reduction of the supernatant by the filter paper (see Electronic Supplementary Information, ESI4),[42] on the upper part of the dried filter cake was analysed *via* ICP-OES. Figure 4 illustrates the temporal variation of both the manganese and the iron in the filter cake, where it is clear that after *ca.* 72 hr of incubation, the manganese level drops by *ca.* 60%, and the iron content decreases by *ca.* 70%. These results are general, and hold irrespective of the origin of the slaked lime feedstock - Northern Province Cretaceous Chalk (derived from a wide range of lithostratigraphies within the Welton Formation) or Carboniferous Limestone (Bee Low Formation). However, there is a subtle difference in the

(a)

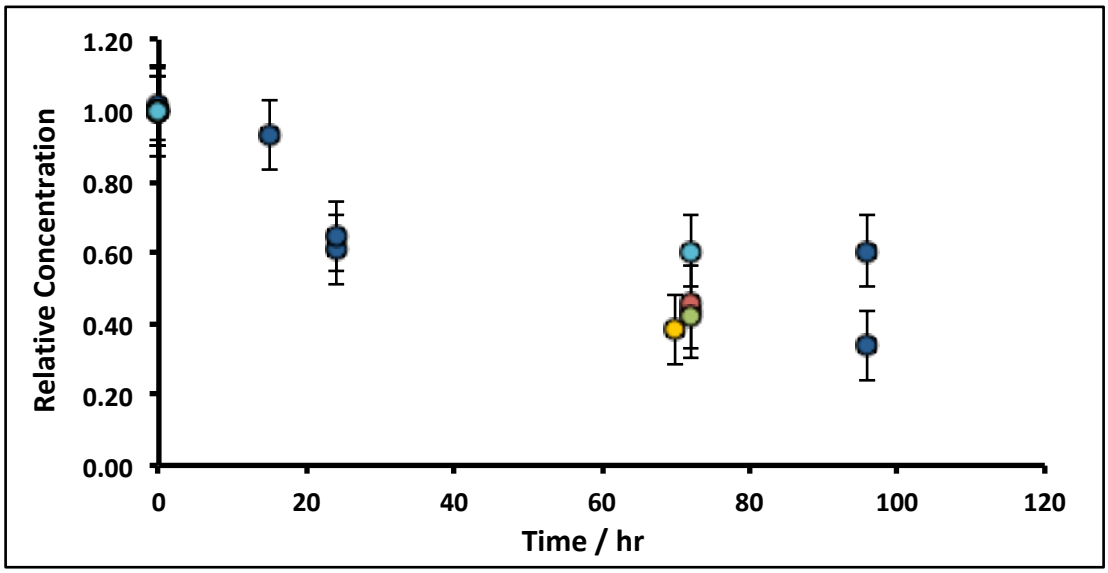

(b)

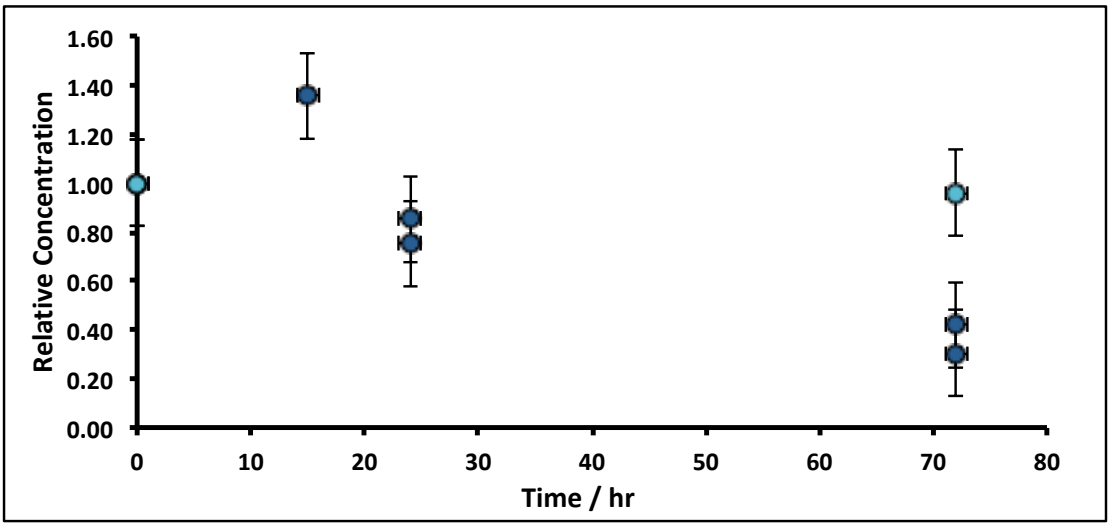

Figure 4: *Variation* of (a) *Mn and (b) Fe under quiescent conditions during incubation with 8% alkaline hypochlorite solution. Note that the data have been normalised to the average manganese or iron level present in untreated sample (when time = 0 hr, and where the relative concentration is unity). Unless stated, experiments were undertaken without oxygen purged-solutions. Key: Dark blue circles correspond to lime hydrate derived from Welton formation Chalk derived from screenings obtained from the middle stratitographic section (between the Melton Ross Marl and the Barton Marl 1); red circles correspond to slaked lime derived from Bee Woo Limestone; green and gold circles correspond to lime hydrate derived from chalk or chalk screenings, respectively, taken from the bottom bed (between the Grasby Marl to just below the Chalk Hill Marl, but above the Black Band); light blue circles correspond to conditions identical to the dark blue circles, except under anærobic (oxygen-purged) conditions. Error bars indicate one standard deviation over at least three samples.*

trends for manganese and iron: the filter cake becomes progressively depleted from manganese impurities during the treatment (irrespective of whether oxygen is present), at an initial rate of ~1%/hr; in contrast, the removal of iron impurities is affected by the presence of oxygen in the solution. Under ærobic conditions, the iron content of the filter cake appears first to increase, and then decrease; however, there is no apparent loss of iron impurity under anærobic conditions.

These results indicate that the removal of both the manganese and the iron impurities occurs in slightly different ways, likely linked to the difference in the oxidation states of the two different transition metal ion impurities, and reaction mechanism. The manganese is present in Mn_3O_4 as both Mn^{II} and Mn^{III}, so that oxidation to Mn^{VII} can be achieved through reaction with alkaline hypochlorite, without requiring the presence of oxygen.

$$2\,Mn_3O_4(s) + 13\,ClO^-(aq) + 6\,OH^-(aq) \longrightarrow 6\,MnO_4^-(aq) + 13\,Cl^-(aq) + 3\,H_2O(\ell) \qquad \text{(A)}$$

This reaction (A) does not have to occur in a single step; rather, since the presence of green Mn^{VI} is noticeable during the filter paper reduction of the supernatant (see Electronic Supplementary Information, ESI4), we may propose the following reaction sequence.

$$\begin{aligned}
&Mn_3O_4(s) + ClO^-(aq) \longrightarrow Mn_2O_3(s) + MnO_2(s) + Cl^-(aq)\\
&Mn_2O_3(s) + ClO^-(aq) \longrightarrow 2\,MnO_2(s) + Cl^-(aq)\\
&MnO_2(s) + ClO^-(aq) + 2\,OH^-(aq) \longrightarrow MnO_4^{2-}(aq) + Cl^-(aq) + H_2O(\ell)\\
&2\,MnO_4^{2-}(aq) + ClO^-(aq) + H_2O(\ell) \longrightarrow 2\,MnO_4^-(aq) + Cl^-(aq) + 2\,OH^-(aq)
\end{aligned} \qquad \text{(B)}$$

This scheme is in agreement with literature observations on the oxidation of manganese species at high pH to afford permanganate.[43] Indeed, we observed that pyrolusite (β-MnO_2) behaved in an analogous manner (data not shown). Note that, in agreement with literature observations for aragonite,[44] we were unable to observe the removal of manganese from chalk immersed in alkaline hypochlorite.

In contrast, since the iron impurities are present as Fe^{III}, the oxidation to afford Fe^{VI} in the presence of concentrated sodium hydroxide (which stabilises the hypochlorite solution) must occur first through the solubilisation of the Fe^{III} species,[45]

$$Fe_2O_3(s) + 2\,OH^-(aq) \longrightarrow 2\,FeO_2^-(aq) + H_2O(\ell) \qquad \text{(C)}$$

In the above, although we have depicted the iron impurities as hæmatite (α-Fe_2O_3), we recognise this could be a different form of Fe^{III}. This solubilisation is also observed as a route for removing iron impurities from aragonite.[44] Indeed, we also observed that maghæmite (γ-Fe_2O_3) was partially solubilised by oxygenated, concentrated sodium hydroxide solution when incubated overnight, affording a pale yellow solution, corresponding to ferrite (data not shown). This is consistent with the low solubility of ferric oxide at ambient temperature,[45] which is reported to increase with both temperature and hydroxide concentration; it has been recognised that the solubility of hæmatite in alkali-metal hydroxide solutions changes with the

alkali metal cation, and follows the order for oxygen oxidation of metallic iron in those solutions.[45b]

In the absence of oxygen, there is little loss of iron from the filter-cake (Figure 5) in the presence of alkaline hypochlorite, suggesting no oxidation takes place. However, in the presence of oxygen, the concentration of iron in the filter-cake first increases (by 40%), and then reduces to close to 60% of the original content. This is suggestive of an oxygen-catalysed Fe^{III} dissolution process: oxygen is not sufficiently strong an oxidant in basic media to oxidise ferrite (FeO_2^-) to ferrate,

$$FeO_2^-(aq) + 4OH^-(aq) \rightleftharpoons FeO_4^{2-}(aq) + 2H_2O(\ell) + 3e^- \quad \text{(D)}$$

However, half-reaction (D) is viable for alkaline hypochlorite: the standard potential for the ferrite/ferrate redox couple, though not very well defined,[43c,45a] is estimated to be ~+0.8 - +0.9 V *vs.* SHE at pH 14. We thus propose that in the absence of oxygen, Fe_2O_3 (or some hydroxylated solid form) remains in the solid state; in the presence of oxygen, adsorption onto the surface of the iron(III) oxide/oxohydroxide first enables solid $NaFeO_2$(s) to form (giving rise to the 40% increase in concentration),[45b,c] which can then dissolve under oxidative conditions to yield the purple ferrate ion in solution. To confirm this, an experiment was undertaken in which magnetite (Fe_3O_4 – a inverse spinel with Fe^{III} in the tetrahedral sites and half of the octahedral sites, with the remaining octahedral sites occupied by Fe^{II}) was incubated with oxygenated, concentrated sodium hydroxide solution. After one week of incubation, the supernatant above the black solid was still clear and colourless; addition of alkaline hypochlorite caused no immediate colour change, except after an overnight incubation, whence the deep purple ferrate anion was observed.

In contrast, experiments using an ironstone (~82% calcite, ~17% gœthite and <1% siderite, see Electronic Supplementary Information, ESI7) refluxed with alkaline hypochlorite did not give rise to a purple solution, indicating the need for ferrite formation to occur through dissolution prior to oxidation.

This confirms the nature of the oxidative etching process of iron-based impurities in lime, which can be written as the overall reaction:

$$Fe_2O_3(s) + 3ClO^-(aq) + 4OH^-(aq) \longrightarrow 2FeO_4^{2-}(aq) + 3Cl^-(aq) + 2H_2O(\ell) \quad \text{(E)}$$

Although no effort was made to shield the solutions from direct sunlight, it is unlikely that photo-reductive dissolution of Fe^{II} by superoxide[46] is viable in these experiments: superoxide is readily oxidised by hypochlorite.

From a chemical process perspective, it is insightful to identify whether the chemical etching process is limited by slow transport of hypochlorite to the slaked lime particle surface, or by slow surface kinetics: in the former case, greater impurity removal will occur with increased

(a)

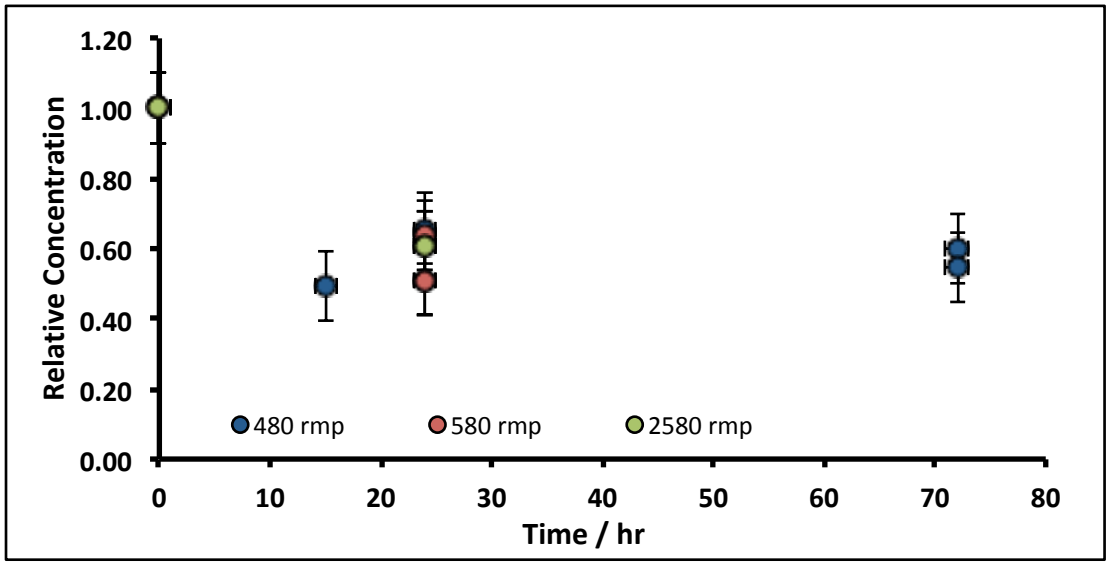

(b)

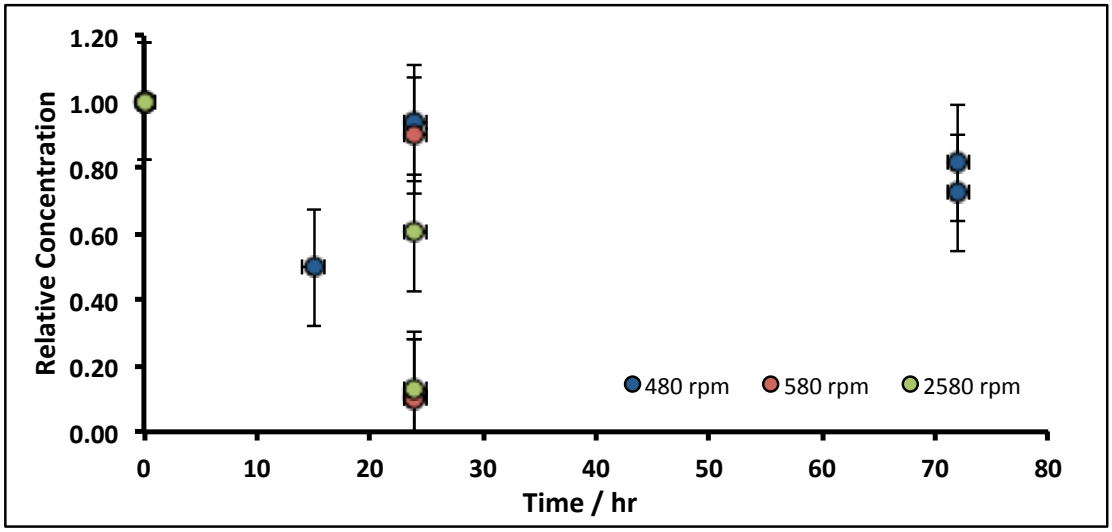

Figure 5: *Variation* of (a) *Mn and (b) Fe under stirred conditions (indicated by the rotation speed of the magnetic flea used) during incubation with 8% alkaline hypochlorite solution. Note that the data have been normalised to the average manganese or iron level present in untreated (and unstirred) sample (when time = 0 hr, and where the relative concentration is unity). All experiments were undertaken under ærobic conditions with lime hydrate derived from Welton formation Chalk derived from screenings obtained from the middle stratitographic section (between the Melton Ross Marl and the Barton Marl 1). Key: Dark blue circles correspond to rotation speeds of 480 rpm; red circles correspond to rotation speeds of 580 rpm; green circles correspond to rotation speeds of 2580 rpm. Error bars indicate one standard deviation over at least three samples.*

agitation of the slaked lime/alkaline hypochlorite slurry; in the latter, greater removal necessitates longer incubation times. The comparison of Figure 5 with Figure 4 indicates that increasing the agitation of the hydrate/hypochlorite solution slurry does not translate into a greater loss of manganese from the resulting filter cake, indicating that the etching is limited by the surface kinetics; this is less evident for the case of iron removal, as expected from the inferred solubilisation prior to oxidation (reaction (E)).

Owing to the control due to slow surface kinetics (50% of impurity removal through chemical etching using alkaline hypochlorite requires between 10-20 hr), reaction variables (such as temperature and hypochlorite concentration) were next varied, so as both to unravel the mechanism further, and to optimise the impurity removal chemistry, in order to develop a more useful and practical process operation.

Optimisation of Dissolutive Process Chemistry

Under ærobic conditions, increasing the temperature from ambient (20 ^{o}C) to 90 ^{o}C in ~8% alkaline hypochlorite solution, causes the initial rate of removal of both manganese and iron impurities in the filter cake to increase to *ca.* 1 %/min (Mn) and *ca.* 3 %/min (Fe), Figure 6. This increase does not results from an apparent increase in solubility: the retrograde solubility of $Ca(OH)_2$ with temperature,[47] in addition to the common-ion effect, serves to reduce hydrate dissolution to negligible values (~0.003 wt.%, see Electronic Supplementary Information, ESI8). Indeed, control experiments using deionised water (1.0 g of lime hydrate equilibrated (20 min at 90 ^{o}C) in 80 mL of deionised water), reveal a 20% increase in the concentration of manganese in the solids, but *ca.* 60% decrease in iron (Figure 6). Inasmuch as an increase in the manganese content is expected: ~5 wt.% of hydrate will dissolve (see Electronic Supplementary Information, ESI8), enriching the impurity concentration, the decrease in iron content of the resulting filter cake is consistent with the formation (and thermally enhanced solubility) of ferrite.[45b] Again, the effect of increasing the mass transport of hypochlorite (higher than that due to thermal convection) has only very limited effect (Figure 6).

The plots in Figure 6 indicate that prolonged incubation at 90 ^{o}C has little effect on the etching. This likely results from the thermal decomposition of hypochlorite, which can be catalysed by ferric oxide, and is thought[48] to proceed *via* a slow initial disproportionation reaction of hypochlorite to chlorite, followed by faster oxidation to chlorate:

$$2ClO^{-}(aq) \longrightarrow ClO_2^{-}(aq) + Cl^{-}(aq)$$
$$ClO^{-}(aq) + ClO_2^{-}(aq) \longrightarrow ClO_3^{-}(aq) + Cl^{-}(aq) \qquad (F)$$

It follows that a *cascade chemical etching* process, where in a batch of slaked lime is treated for a fixed, short period of time (intervals of 1, 2 and 3 hr) at 90 ^{o}C with alkaline hypochlorite, filtered and then re-treated using fresh hypochlorite reagent under the same conditions, would

(a)

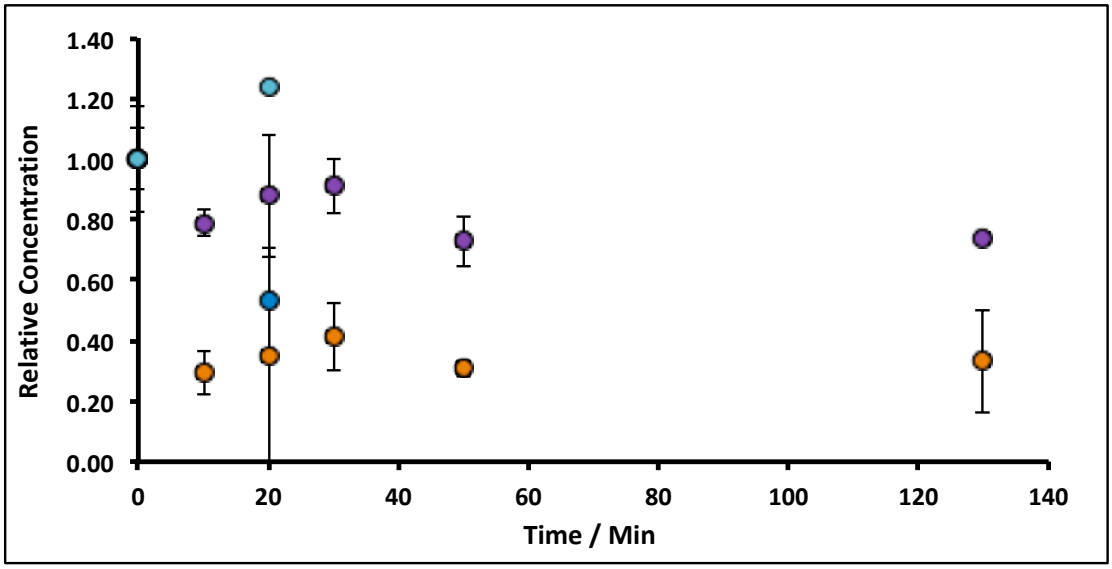

(b)

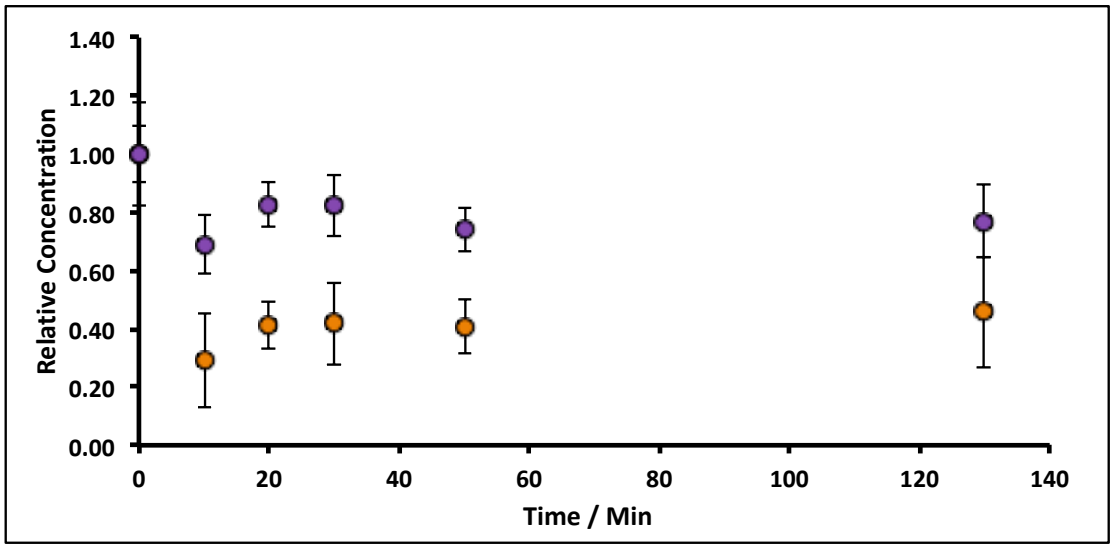

Figure 6: *Variation* of *Mn and Fe concentrations in lime hydrate filter cake during incubation with 8% alkaline hypochlorite solution or deionised water at 90 °C, under (a) non-stirred but thermally convective, and (b) stirred at an arbitrary rotation speed of the magnetic flea used. Note that the data have been normalised to the average manganese or iron level present in untreated (and unstirred) sample (when time = 0 hr, and where the relative concentration is unity). All experiments were undertaken under ærobic conditions with lime hydrate derived from Welton formation Chalk derived from screenings obtained from the middle stratitographic section (between the Melton Ross Marl and the Barton Marl 1). Key: purple circles correspond to Mn concentrations using alkaline hypochlorite solution; sky blue circles correspond to Mn concentration using deionised water; orange circles correspond to Fe concentrations using alkaline hypochlorite solution; blue circles correspond to Fe concentration using deionised water. Error bars indicate one standard deviation over at least three samples.*

(a)

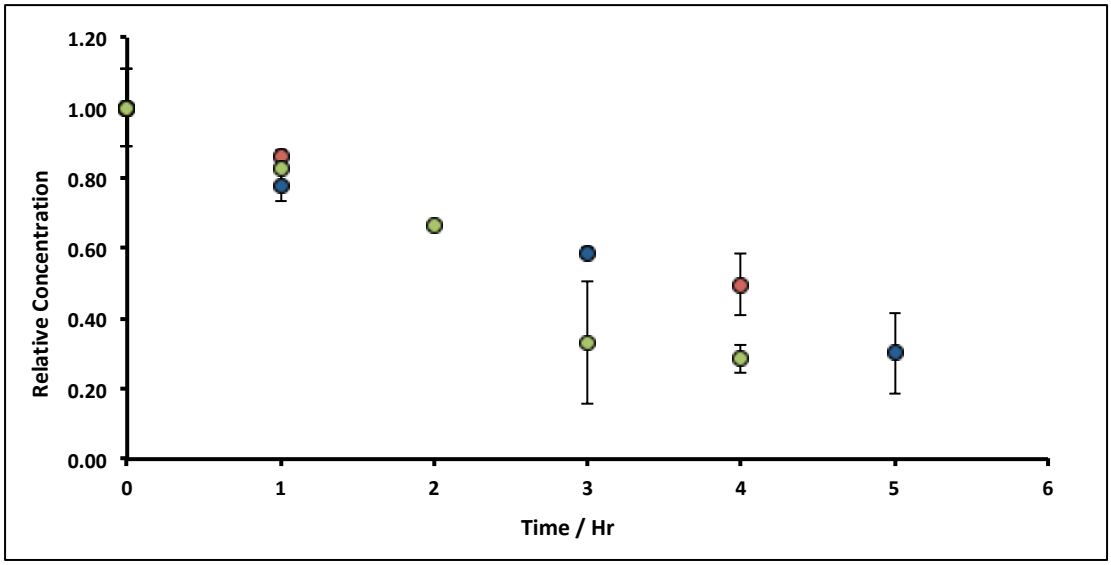

(b)

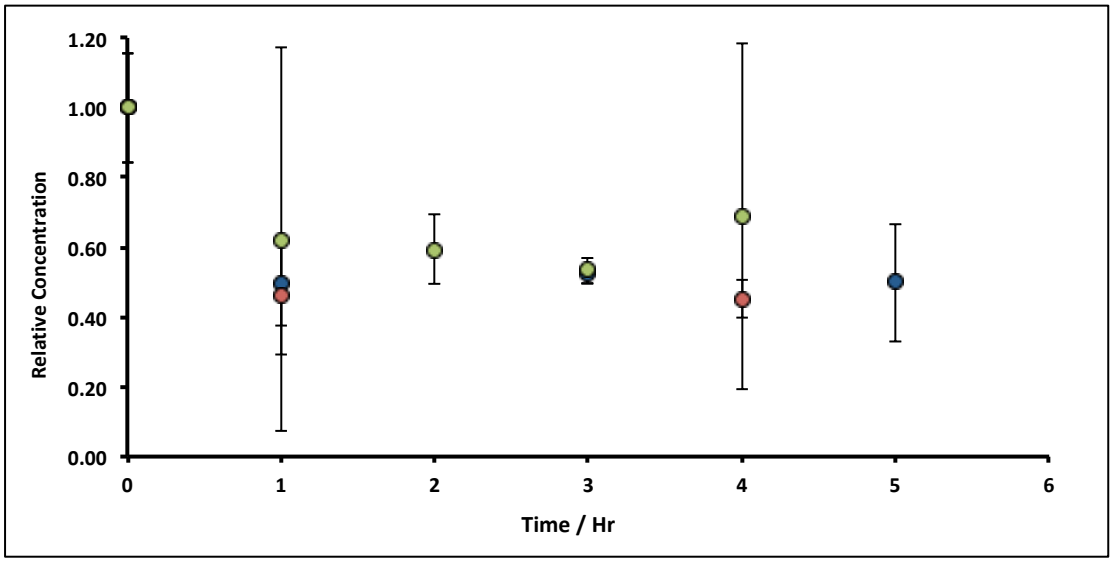

Figure 7: *Variation of (a) Mn and (b) Fe concentrations in lime hydrate filter cake during variable time incubation intervals (1, 2 and 3 hr) with 8% alkaline hypochlorite solution or deionised water at 90 ^{o}C whilst stirred at an arbitrary rotation speed of the magnetic flea used. Note that the data have been normalised to the average manganese or iron level present in untreated (and unstirred) sample (when time = 0 hr, and where the relative concentration is unity). All experiments were undertaken under ærobic conditions with lime hydrate derived from Welton formation Chalk derived from screenings obtained from the middle stratitographic section (between the Melton Ross Marl and the Barton Marl 1). Key: green, blue and red circles correspond to incubation times of 1, 2 and 3 hr, respectively. Error bars indicate one standard deviation over at least three samples.*

(a)

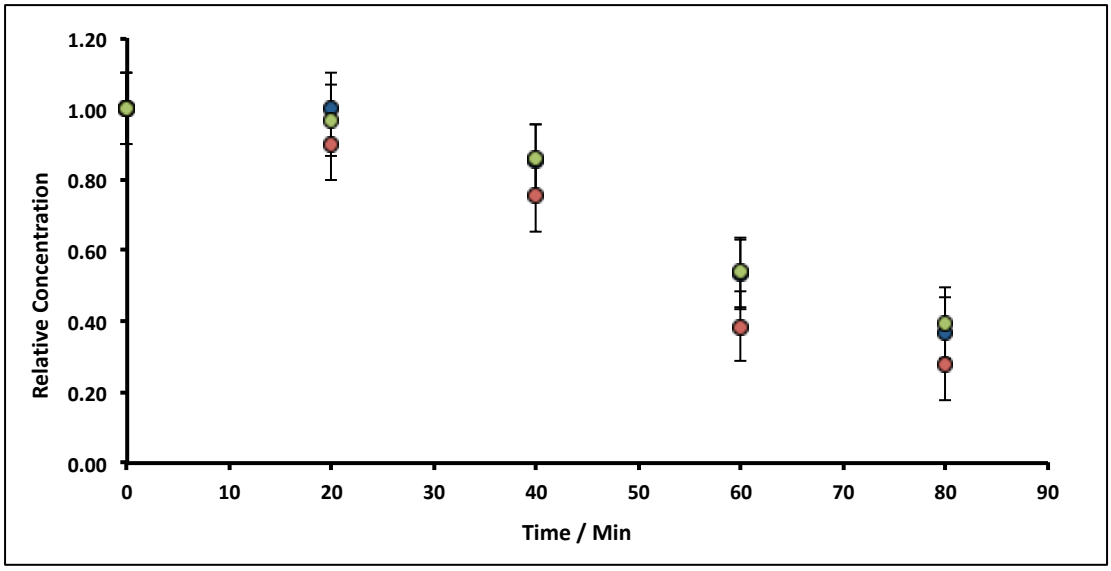

(b)

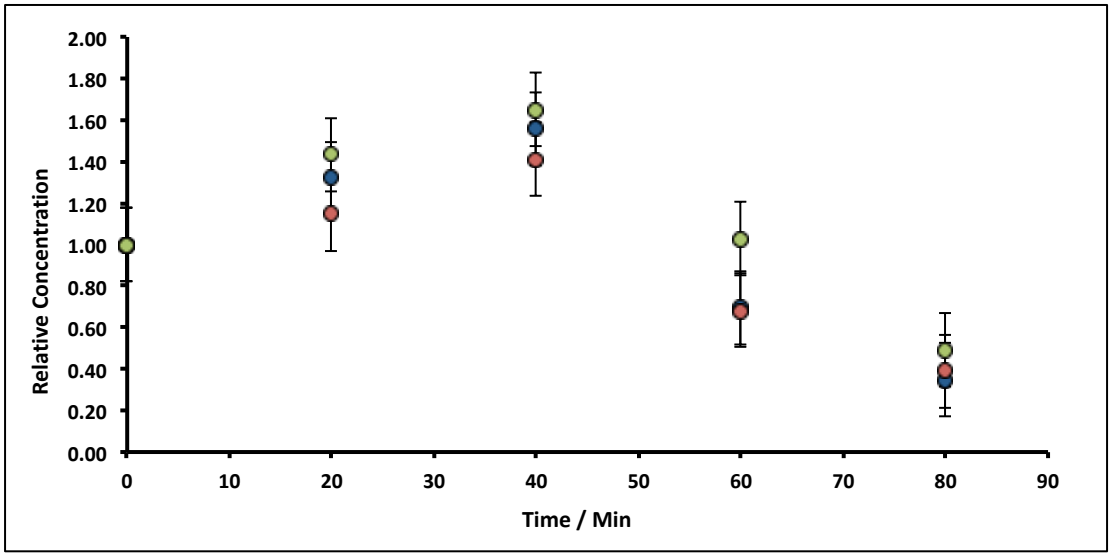

Figure 8: *Variation of (a) Mn and (b) Fe concentrations in lime hydrate filter cake during fixed 20 min incubation cascades with 8% or 14% alkaline hypochlorite solution or deionised water at 90 ^{o}C whilst stirred at an arbitrary rotation speed of the magnetic flea used. Note that the data have been normalised to the average manganese or iron level present in untreated (and unstirred) sample (when time = 0 hr, and where the relative concentration is unity). All experiments were undertaken under ærobic conditions with lime hydrate derived from Welton formation Chalk derived from screenings obtained from the middle stratitographic section (between the Melton Ross Marl and the Barton Marl 1). Key: blue, red and green circles correspond to hypochlorite chloride levels of 8% (batch 1), 8% (batch 2) and 14%, respectively. Error bars indicate one standard deviation over at least three samples.*

enable *shorter* treatment times and, overall *faster* impurity removal. This is indeed observed, as illustrated in Figures 7 and 8, where it is appreciated that the initial rate of removal with fresh hypochlorite solution is maintained though this staged process. Moreover, as expected, the shortest cascade incubation (20 min) soonest yields the purest filter cake (Figure 8) in terms of manganese and iron removal. Again, the contrast between the iron and the manganese data is likely due to the requirement to solubilise the iron species as ferrite, especially at the higher temperature, suggesting that this first step (assisted by oxygen) is rate-determining for iron impurity removal at the higher temperature.

Under these conditions of temperature (90 ^{o}C) and cascade interval (20 min), increasing the hypochlorite concentration from ~8% to ~14% (a concentration factor of 1.75), has little effect on the removal of manganese or iron (Figure 8). This indicates that removal of both manganese and iron follows zeroth-order kinetics in hypochlorite in both cases. Focussing on the mechanistically less complicated manganese dissolution, the manganese-removal rate,

$$\frac{d\left(n_{Mn}\right)_{solid}}{dt} = -k_{het} \qquad (1)$$

where $\left(n_{Mn}\right)_{solid}$ is the number of moles of manganese in the solid lime hydrate (virgin material or filter-cake) to which alkaline hypochlorite solution is added, and k_{het} is the zeroth-order rate constant corresponding to the rate-limiting step in the sequence of steps provided in reaction (B) – see also Electronic Supplementary Information, ESI9. The solid manganese concentration determined using ICP-OES (see Electronic Supplementary Information, ESI4) affords manganese concentrations as parts-per-million by mass (ppm, mg/kg), so that at any time t, $\left(n_{Mn}\right)_{solid}^{t} = \frac{10^{-6}\left(ppm\right)^{t}\left\{m_s - qsV\right\}}{M_{Mn}}$, in which $(ppm)^t$ is the manganese concentration in the filter-cake, m_s is the mass of the virgin lime hydrate used at the start of the experimental cascade (in g), s is the solubility of the lime hydrate in the alkaline solution at the experimental temperature (in g/L), V is volume of the alkaline hypochlorite solution used (in L), which is kept at a constant value throughout the cascade, q is the cascade number, with the first batch taking q = 1, and M_{Mn} is the molar mass of manganese (in g/mol). This enables equation (1) to be re-cast in terms of the solid manganese concentration, and integrated using the boundary condition t = 0, $(ppm)^t = (ppm)^0$, to yield equation (2):

$$\frac{\left(ppm\right)^{t}}{\left(ppm\right)^{0}} = 1 - k_{eff}t \qquad (2)$$

in which the effective rate constant, $k_{eff} = k_{het}\frac{10^{6} M_{Mn}}{\left(ppm\right)^{0}\left\{m_s - qsV\right\}}$. For the extremely low lime hydrate solubilities (for further discussion, see Electronic Supplementary Information, ESI8 and ESI9), the corrected mass is essentially constant, so that plots of relative manganese concentration against time are linear, as observed in Figure 9 for small cascade numbers. These afford values of k_{het} = 6.1 ± 1.5 × 10^{-8} mol/min at 90 ^{o}C for the removal of manganese

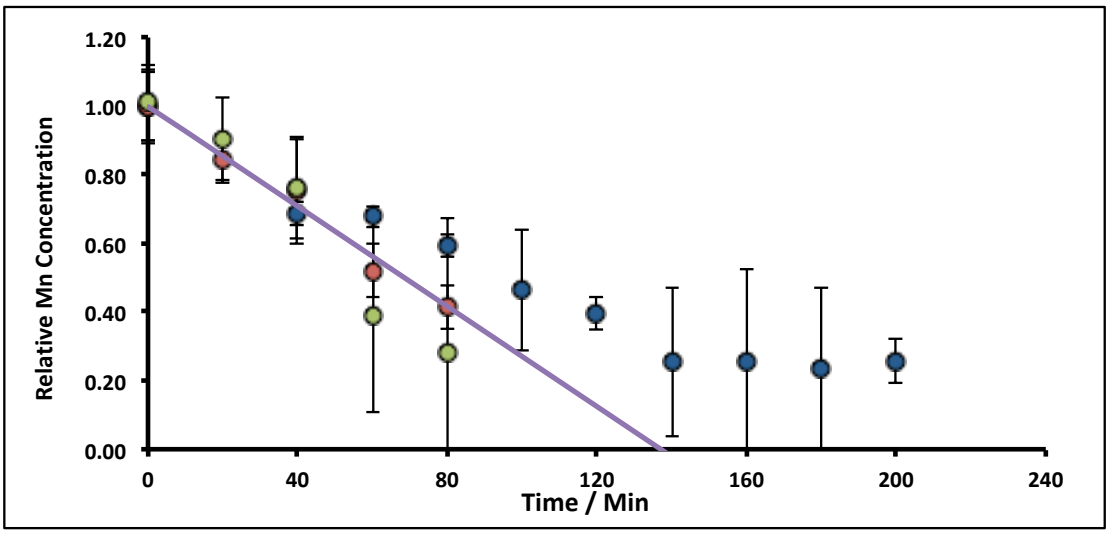

Figure 9: *Variation of Mn concentrations in lime hydrate filter cake during fixed 20 min incubation cascades with 14% alkaline hypochlorite solution or deionised water at 90 ^{o}C whilst stirred at an arbitrary rotation speed of the magnetic flea used. Note that the data have been normalised to the average manganese or iron level present in untreated (and unstirred) sample (when time = 0 hr, and where the relative concentration is unity). All experiments were undertaken under ærobic conditions. Blue and green circles correspond to lime hydrate derived from Welton formation Chalk derived from screenings obtained from the middle stratitographic section (between the Melton Ross Marl and the Barton Marl 1), with initial hydrate mass of 2.0 and 1.0 g, respectively; red circles correspond to lime hydrate derived from Carboniferous Limestone, with initial hydrate mass of 1.0 g. Error bars indicate one standard deviation over at least three samples. The purple line corresponds to equation (2), with the average effective rate constant, k_{eff} = 7.3 ± 1.9 x 10^{-3} min^{-1}.*

impurities in lime hydrate, which are independent of both the derived limestone type (Cretaceous Chalk or Carboniferous Limestone), and the mass of the material treated, suggesting all samples are approximately monodisperse and with similar particle sizes.

For manganese removal, these are *pure kinetics* – they have no contribution from mass transfer: under the approximation that the Sherwood number (Sh) is 2, *viz.*,[49] $Sh = \frac{d_p k_L}{D} = 2$, an equation relevant for mass transfer to small particles, where d_p is the slaked lime particle diameter (5 μm),[36] D is the diffusion coefficient of hypochlorite in aqueous alkaline solution (~10^{-5} cm^2 s^{-1}), the mass transfer coefficient (k_L) is estimated as being 0.04 cm/s. In the experiments in Figure 9, the etching rate constant at 90 ^oC is ~ 10^{-9} mol/s from a surface area of[36] ~20 m^2/g using an hypochlorite concentration of ~5 M, affording a mass transfer coefficient of ~10^{-12} cm/s, which is many orders of magnitude less than the transport-limited rate, confirming no contribution from mass transfer.[50]

The low temperature data illustrated in Figure 4 can also be analysed through equation (2), to afford k_{het} = 8.0 ± 3.4 × 10^{-10} mol/min at 20 ^oC for manganese removal from lime hydrate. Again, this is independent of the derived limestone type, and whether the etching is undertaken in the presence, or absence of oxygen. These low and high temperature rate constants enable the estimation of the activation barrier for the etching process to be 0.58 ± 0.07 eV, using an Arrhenius-type relationship. This activation energy is similar to literature estimates for the DC conductivity (*via* electron hopping between Mn^{II} and Mn^{III} sites) within nano-crystalline (~10 nm) Mn_3O_4 (0.45-0.69 eV),[51] and suggests that the slow step for manganese etching is an interfacial electron transfer event:

$$Mn_3O_4(s) + ClO^-(aq) \xrightarrow{slow} Mn_2O_3(s) + MnO_2(s) + Cl^-(aq) \qquad (G)$$

where the manganese impurities remain in the solid state, during inner-sphere oxidation[52] by hypochlorite ions across the solid/liquid interface.

In order to confirm the dissolution rate as being controlled by an interfacial electron transfer process, ambient temperature experiments were undertaken in which the chemical oxidant was replaced by distilled water saturated with both ozone and lime hydrate (pH 12.3). In this case (data not shown), the value of k_{het} was observed to be 2.2 ± 0.1 × 10^{-8} mol/min (when corrected for the greater solubility of lime hydrate in water than in sodium hydroxide solution). This value is significantly larger than that observed at ambient temperature for alkaline hypochlorite oxidants, even after accounting for the concentration differences[53] between ozone (at saturation, ~5 mM) and the hypochlorite solution used (~2.5 M). Nevertheless, these results are consistent with the expected linear free energy nature of the activation/driving force within the normal Marcus region:[54] the standard potentials at[45a] pH 14, E^0_B = +1.24 V *vs.* SHE (for O_3/O_2), with E^0_B = +0.89 V *vs.* SHE (for ClO^-/Cl^-) confirm the

greater oxidising strength of ozone compared with hypochlorite, and, thence, the faster dissolution rate in the presence of ozone.

The observation of zeroth-order kinetics for manganese loss from slaked lime gives rise to a "rule-of-thumb" for the scale-up of this process chemistry. However, it is important to realise that after removal of *ca.* 75% of the original manganese impurity, a constant amount remains, as determined *via* ICP-OES (Figure 9). This is "inactive" manganese – it is inaccessible and cannot be removed through a chemical etch with hypochlorite – either because it is too deep within the core of the hydrate particles (within the 3% calcite), or because it is in a different "shell" of the hydrate, or even in a different oxidation form, compared with the "active manganese", and thus has a slower etching rate constant.

We next consider how the insights into this chemical etching chemistry can adapted to existing processes where lime is used for the drinking water distribution network.

Adaptation for End-use

Current methods the removal of soluble iron and manganese in drinking water typically uses elaborate filtration beds, each with a unit treatment cost of €0.12/m^3 (for a mid-sized water treatment plant).[9] The removal of iron or manganese in drinking water treatment chemicals is not a standard practice, so that implementation of corrective actions, such as those indicated herein, necessarily has to be of low cost. Given this, considering typical water treatment plants employ pH modifiers such as lime, and oxidative disinfection chemicals such as chlorine or hypochlorite at a number of process stages, "manganese-free" lime is only needed if there is no filtration bed after the last combination of lime and oxidant. This reduces the demand for "manganese-free" lime.

The chemical etching pathway demonstrated herein suffers from slow, zeroth-order heterogeneous kinetics, and this requires process heat to raise the temperature to 90 ^{o}C. However, these high temperatures facilitate the decomposition of the alkaline oxidant required, so that a cascade approach is required, if hypochlorite is used as the oxidant, which adds to the overall operational expenditure required: this work has demonstrated capability only using at a solid hydrate to liquid solution oxidant ratio of between 0.0125 - 0.025 g/mL. Whilst further work may be able to demonstrate viability through increasing this ratio, an alternative is to employ the use of a different oxidant, such as the continual bubbling of chlorine gas in an aqueous lime slurry ("aqualime"). Although lime manufacturers do distribute aqualime, they tend not to have chlorine gas on-site. However, water treatment plants typically have opportunities to make aqualime on-plant, and sometimes may have the process safety infrastructure needed to use chlorine on-plant, so that water companies may use this chemistry. An additional advantage of performing this chemistry on a water treatment plant is that the permanganate and ferrate generated can be used to remove the

odour associated with reduced gases (such as hydrogen sulphide and ammonia) that are typically present on such sites.

Conclusions

In this work, we have developed high pH redox chemistry that demonstrates how both manganese and iron impurities can be removed from lime hydrate derived from quarried limestones. The mechanism for the oxidative removal is different for both iron and manganese: in the former, oxygenated solutions are required to transform the surface ferric oxide into ferrite, which can be solubilised through oxidation with hypochlorite to yield soluble ferrate; in contrast, hausmannite is oxidised stepwise by hypochlorite (or ozone), ultimately to furnish soluble permanganate.

These reactions are under activation control, with the kinetics of oxidation increasing with temperature. For manganese, these dissolution kinetics are zeroth-order that appear to be limited by the rate of electron transfer, enabling design rules for the up-scale of this process to be determined of ~1%/min for manganese and ~3%/min for iron, at 90 ^{o}C. However, it is important to realise that this chemistry cannot create a completely "manganese-free" or "iron-free" product: around 25% of the total manganese ("inactive" manganese) remains, irrespective of the feedstock (Carboniferous Limestone or Cretaceous Chalk).

Although further work is needed to examine the economic viability of this process chemistry at scale, it nevertheless provides an opportunity for manufacturers to develop suitable lime hydrate products that hold very low levels of manganese and iron impurities. Alternatively, given the simplicity of the operations, and that the treatment chemicals are similar to those already deployed for disinfection in the water industry, the impurity-removal process could potentially be integrated on the site of existing water treatment works.

Last, we note that control of manganese in lime products is important for processes other than in those employed by the water industry.[55-57]

Acknowledgements

This work was funded by Singleton Birch, Ltd. (50%), together with InnovateUK (25%) and the Engineering and Physical Sciences Research Council (25%), through a Knowledge Transfer Partnership (Programme Number 0110770). DK thanks The University of Hull for funding his MSc research studentship. RAW thanks Singleton Birch for funding. We thank Haydn Ward (ParagonID) for the generous donation of both magnetite and maghæmite used in this work, Pauline Smedley (British Geological Survey) for arranging access to reference S25, and Bernadette Ryan (Severn Trent, Plc) and Anna Taliana (Dŵr Cymru Welsh Water)

for useful discussions. DK, NSL and JDW thank the Johnston Quarry Group for generously supplying a sample of Great Tew Ironstone. We are grateful to two anonymous reviewers who have improved the flow of this manuscript.

Conflicts of Interest

DK and CRM are both employed by Singleton Birch, Ltd.

CRediT Statement

Conceptualisation: DK, CRM, NSL, JDW
Methodology: DK, CRM, NSL, JDW
Investigation: DK
Formal analysis: DK, CRM, NSL, JDW
Software: DK, JDW
Validation: DK, RAW
ICP-OES: MT
X-Ray diffraction and analysis: TJP
Resources: DK, CRM, SMK, NSL, JDW
Data curation: DK, CRM, JDW
Writing – original draft: DK, CRM, NSL, JDW
Writing – review and editing: DK, RAW, CRM, MT, TJP, SMK, NSL, JDW
Visualisation: DK, CRM, NSL, JDW
Supervision: DK, CRM, NSL, JDW
Project administration: CRM, NSL, JDW
Funding acquisition: CRM, SMK, NSL, JDW

References and Notes

1. See, for example, United Nations General Assembly Resolution 64/292: *The Human Right to Water and Sanitation*, United Nations, adopted July 28, 2010.
2. E. C. Craig, E. L. Bean, R. W. Sawyer, Iron and lime in removal of manganese, *J. Am. Water Works Assoc.*, 1932, **24**, 1762.
3. The complexity of the water distribution and regulatory framework in the United Kingdom is elegantly captured in a recent speech by Sir James Bevan, Chief Executive of the Environment Agency, *Escaping the Jaws of Death: Ensuring Enough Water in 2050*, Waterwise Conference, March 19, 2019; full transcript available at the following URL. https://www.gov.uk/government/speeches/escaping-the-jaws-of-death-ensuring-enough-water-in-2050 (Accessed December 28, 2021).
4. World Heath Organisation, *Guidelines for Drinking Water Quality*, 4th edn. (incl. 1st add.), World Heath Organisation, Geneva, 2017.
5. See, for example, D. K. Todd, L. W. Mays, *Groundwater Hydrology*, 3rd edn., Wiley, New Delhi, 2005.
6. (a) For example, the chalk aquifer of the East Riding of Yorkshire is contaminated by both atrazine (a pesticide) and dichloromethane (a non-aqueous phase liquid) at concentrations above European guideline values, *q.v.* I. N. Gale, H. K. Rutter, *The Chalk Aquifer of Yorkshire*, British Geological Survey Research Report RR/06/04, British Geological Survey, Keyworth, 2006; (b) Likewise, "forever chemicals" such as perfluorinated hydrotopes have been found in soils, surface waters and groundwaters throughout England: see, for example, E. Pemberton, *Poly- and Perfluoroalkyl Substances (PFAS): Sources, Pathways and Environmental Data*, Chief Scientist's Report, Environment Agency, Bristol, 2021.
7. (a) J. Fawell, M. J. Nieuwenhuijsen, Contaminants in drinking water, *Br. Med. Bull.*, 2003, **68**, 199; (b) S. Sharma, A. Bhattacharya, Drinking water contamination and treatment techniques, *Appl. Water Sci.*, 2017, **7**, 1043.
8. (a) S. Zahran, D. Mushinski, S. P. McElmurry, C. Keyes, Water lead exposure risk in Flint, Michigan after switchback in water source: implications for lead service line replacement policy, *Environ. Res.*, 2020, **181**, 108928; (b) K. J. Pieper, M. Tang, M. A. Edwards, Flint water

crisis caused by interrupted corrosion control: investigating “ground zero” home, *Environ. Sci. Technol.*, 2017, **51**, 2007.
9. A. Postawa, C. Hayes (eds.), *Best Practice Guide on the Control of Iron and Manganese in Water Supply*, IWA Publishing, London, 2013.
10. Drinking Water Inspectorate, *Drinking Water 2020: The Chief Inspector’s Report for Drinking Water in England*, Drinking Water Inspectorate, London, 2021.
11. (a) V. A. Pattinson, D. P. Butcher, J. C. Labadz, J. Shacklock, Water discolouration and the ôô of the reservoir, *Phys. Chem. Earth*, 1995, **20**, 175; (b) S. Buss, *Review of Spatial Factors Controlling Water Discolouration in England and Wales*, Appendix 10, Technical Note 64116BN TN1D1, ESI, Ltd., 2018.
12. (a) L. I. Sly, M. C. Hodgkinson, V. Arunpairojana, Deposition of manganese in a drinking water distribution system, *Appl. Environ. Microbiol.*, 1990, **56**, 628; (b) J. M. Cerrato, L. P. Reyes, C. N. Alvarado, A. M. Dietrich, Effect of PVC and iron materials on Mn(II) deposition in drinking water distribution systems, *Water Res.*, 2006, **40**, 2720; (c) J. H. H. Vreeburg, J. B. Boxall, Discolouration in potable water distribution systems: a review, *Water Res.*, 2007, **41**, 519.
13. (a) For a thorough discussion of process improvements suggested by Severn Trent to improve their distribution of soft water, derived from the Elan Valley catchment in Wales, to the City of Birmingham (maximum flow of 450 ML/day), so as to reduce the iron, manganese, colour, turbidity and natural aluminium levels, see T. Schofield, R. Perkins, J. S. Simms, Frankley Water Treatment Works redevelopment: pilot-scale studies, *Water Environ. J.*, 1991, **5**, 370; (b) A. E. Griffin, Significance and removal of manganese in water supplies, *J. Am. Water Works Assoc.*, 1960, **52**, 1326.
14. S-W. Lee, M. Jones, C. Romano, B. M. Tebo, Formation of manganese oxide minerals by bacteria, in I. A. M. Ahmed, K. A. Hudson-Edwards (eds.), *Redox-Reactive Minerals: Properties, Reactions and Applications in Natural Systems and Clean Technologies*, EMU Notes in Mineralogy, volume 17, chapter 7, The Mineralogical Society of Great Britain and Ireland, London, 2017, p, 173.
15. D. Dixon, N. Anderson, B. Bolto, B. Chiswell, L. Sly, T. Hurse, K. Craig, G. Hamilton, B. Hutchinson, C. West, R. Woolley, *The Removal of Manganese from Drinking Waters*, Research Report No. 26, The Co-operative Research Centre for Water Quality and Treatment, Salisbury, Australia, 2006.
16. (a) We note that recent laboratory-scale research[16b] has illustrated how Mn^{2+} (at concentrations of 2 ppm in 0.1 M aqueous phosphate buffer) can be removed as Mn_2O_3 (lowering the aqueous concentration to *ca.* 900 ppb) *via* advanced electrochemical oxidation, although this technology has yet to be assessed for technical, environmental and economic feasibility; (b) S. T. McBeath, D. P. Wilkinson, N. J. D. Graham, Advanced electrochemical oxidation for the simultaneous removal of manganese and generation of permanganate oxidant, *Environ. Sci.: Water Res. Technol.*, 2020, **6**, 2405.
17. (a) G. Dillon, P. Jackson, A. Ewence, J. Jonsson, *Potential Contaminants in Drinking Water Treatment Chemicals: Final Report to the Department for the Environment, Food and Rural Affairs*, Report No. Defra9033.03, WRc, plc, Swindon, 2003; (b) Note that in the USA, similar standards are in operation, see NSF/ANSI 60-2016, *Drinking Water Treatment Chemicals – Health Effects*, NSF International, Michigan, 2016; (c) P. Rumsby, H. Clegg, J. Jonsson, V. Benson, M. Harman, T. Doyle, L. Rushton, P. Warwick, D. Wilkinson, *Speciation of Manganese in Drinking Water: Final Report for the Drinking Water Inspectorate*, Report No. DWI70-2-276, WRc, plc, Swindon, 2014.
18. (a) S. R. Jenkins, L. Benefield, M. J. Keal, R. S. Peacock, Effective manganese removal using lime as an additive, *J. Am. Water Works Assoc.*, 1984, **76**, 82; (b) A. M. Silva, F. L. S. Cruz, R. M. F. Lima, M. C. Teixeira, V. A. Leão, Manganese and limestone interactions during minewater treatment, *J. Hazard. Mater.*, 2010, **181**, 514; (c) D. L. Trollip, J. C. Hughes, L. W. Titshall, Sources of manganese in the residue from a water treatment plant, *Water SA*, 2013, **39**, 265.
19. (a) A. Hamdouni, G. Montes-Hernandez, M. Tlili, N. Findling, F. Renard, C. V. Putnis, Removal of Fe(II) from groundwater *via* aqueous portlandite carbonation and calcite-solution interactions, *Chem. Eng. J.*, 2016, **283**, 404; (b) A. Sdiri, T. Higashi, T. Hatta, F. Jamoussi, N. Tase, Removal of heavy metals from aqueous solution by limestone, *Intl. J. Global Environ. Issues*, 2012, **12**, 171; (c) B. I. Whittington, The chemistry of CaO and $Ca(OH)_2$ relating to the Bayer process, *Hydrometallurgy*, 1996, **43**, 13.
20. (a) S. Caserini, N. Storni, M. Grosso, The availability of limestone and other raw materials for ocean alkalinity enhancement, *Global Biogeochem. Cycles*, 2022, **36**, e2021GB007246.; (b) J. Hartmann, N. Moosdorf, The new global lithological map database GLiM: a representation of rock properties at the Earth surface, *Geochem. Geophys. Geosys.*, 2012, **13**, 1.
21. (a) Data taken from (i) *USGS Mineral Commodity Summaries 2022*, U.S. Geological Survey, Reston, Virginia, 2022, and (ii) the associated data release for the 2020 tables, available to download at https://www.usgs.gov/centers/national-minerals-information-center/lime-statistics-and-information, accessed January 6, 2023; (b) This is in agreement with the proportion of end-use of ground calcium carbonate (9%) used for environmental protection (flue gas,

drinking water and sewage treatment) reported in European Commission, *Report on Critical Raw Materials for the EU: Non-Critical Raw Materials Profiles*, 2014, Reference: Ares(2014)3690319-06/11/2014.

22. (a) Department of the Environment, *Appraisal of High-Purity Limestones in England and Wales: A Study of Resources, Needs, Uses and Demands: Summary Report*, Department of the Environment, London, 1990; (b) D. J. Harrison, J. M. Hudson, B. Cannell, *Appraisal of High-Purity Limestones in England and Wales: A Study of Resources, Needs, Uses and Demands: Part 1: Resources*, British Geological Survey Mineral Resources Series WF/90/10, British Geological Survey, Keyworth, 1991; (c) D. J. Harrison, High-purity limestones in England and Wales, *Quart. J. Eng. Geol.*, 1993, **26**, 293; (d) D. J. Harrison, D. Highley, A. Bloodworth, R. Bate, D. Cameron, P. Lusty, D. Rayner, *Limestone*, Mineral Planning Factsheet prepared for the Office of the Deputy Prime Minister, British Geological Survey, Keyworth, 2006, available to download from http://www.mineralsUK.com (accessed December 28, 2021); (e) C. Mitchell, High-purity limestone quest, *Industrial Minerals*, 2011, 48.
23. The British Lime Association (one of the constituent bodies of the Mineral Products Association) is the trade organisation for the companies that are responsible for producing at least 75% (*ca.* 1.2 MTe/yr) of the industrial lime sold in the UK: http://www.britishlime.org (accessed December 28, 2021). The British Calcium Carbonate Federation is the trade body representing the interests of UK producers and suppliers of chalk, limestone, marble, dolomite and precipitated calcium carbonate, whose members produce >3.5 MTe/yr of calcium carbonate products: http://www.calciumcarbonate.org.uk (accessed December 28, 2021).
24. (a) G. D. Gaunt, T. P. Fletcher, C. J. Wood, *Geology of the Country Around Kingston-upon-Hull and Brigg: Memoir for 1:50000 geological sheets 80 and 89 (England and Wales)*, British Geological Survey, Her Majesty's Stationary Office, London, 1992; (b) F. Whitham, The geology of the Melton Ross chalk quarries, *Humber Geologist*, No. 12, Hull Geological Society, Kingston-upon-Hull, 1999, available online: http://www.hullgeolsoc.co.uk/meltonrs.htm (accessed December 28, 2021).
25. (a) D. J. Harrison, *The Limestone and Dolomite Resources of the Country Around Buxton, Derbyshire: Description of 1:25000 sheet SK 07 and parts of SK 06 and 08*, Mineral Assessment Report 77 for the Institute of Geological Sciences, Her Majesty's Stationary Office, London, 1981; (b) D. J. Harrison, K. A. McL. Adlam, *Limestones of the Peak: A Guide to the Limestone and Dolomite Resources of the Peak District of Derbyshire and Staffordshire: Description of parts of 1:50000 geological sheets 99, 111, 112, 124 and 125*, Mineral Assessment Report 144 for the British Geological Survey, Her Majesty's Stationary Office, London, 1985.
26. (a) F. C. Cox, D. McC. Bridge, J. H. Hull, *Procedure for the Assessment of Limestone Resources*, Mineral Assessment Report for the Institute of Geological Sciences, No. 30, Her Majesty's Stationary Office, London, 1977; (b) D. J. Harrison, *Industrial Minerals Laboratory Manual: Limestone*, Mineralogy and Petrology Series Technical Report WG/92/29, British Geological Survey, Keyworth, 1993; (c) D. J. Harrison, S. D. J. Inglethorpe, C. J. Mitchell, S. J. Kemp, P. Chaodumrong, M. Charusribandhu, *Procedures for the Rapid Assessment of Limestone Resources*, Overseas Geology Series Technical Report WC/98/1, British Geological Survey, Keyworth, 1998.
27. R. S. Boynton, *Chemistry and Technology of Lime and Limestone*, 2nd edn., John Wiley and Sons, New York, 1980.
28. (a) W. M. Edmunds, W. G. Darling, D. G. Kinniburgh, L. Dever, P. Vachier, *Chalk Groundwater in England and France: Hydrogeochemistry and Water Quality*, British Geological Survey Research Report SD/92/2, Keyworth, 1992; (b) Whilst limestone rocks are generally known to give rise to karstland that characterised geomorphological features including caves, sink holes and dolines, the non-karstic nature of chalk landscapes has been challenged recently – see L. Maurice, A. R. Farrant, E. Mathewson, T. Atkinson, Karst hydrogeology of the Chalk and implications for groundwater protection, in R. P. Farrell, N. Massei, A. E. Foley, P. R. Howlett, J. J. West (eds.), *The Chalk Aquifers of Northern Europe*, Geological Society Special Publications volume 517, Geological Society, London, in press: DOI: 10.1144/SP517-2020-267.
29. P. Shand, J. Bloomfield, *Mineralisation of Shallow Fracture Surfaces in the Chalk and Implications for Contaminant Attenuation*, British Geological Survey Hydrology Series Technical Report WD/95/15, British Geological Survey, Keyworth, 1995.
30. I. Casas, D. Casabona, L. Duro, J. de Pablo, The influence of hæmatite on the sorption of uranium(VI) onto granite filling fractures, *Chem. Geol.*, 1994, **113**, 319.
31. O. Landström, E. L. Tulborg, *The Influence of Fracture Mineral/Groundwater Interaction on the Mobility of U, Th, REE and Other Trace Elements*, SKB (Swed. Nucl. Fuel & Waste Manage. Co.) , Technical Report 90-37, Stockholm, 1990.
32. K. A. Hudson-Edwards, D. Kossoff, Rôle of redox-reactive minerals in the re-use and remediation of mine wastes, in I. A. M. Ahmed, K. A. Hudson-Edwards (eds.), *Redox-Reactive Minerals: Properties, Reactions and Applications in Natural Systems and Clean* Technologies,

EMU Notes in Mineralogy, volume 17, chapter 12, The Mineralogical Society of Great Britain and Ireland, London, 2017, p. 357.
33. (a) F. C. Cox, D. Mac. Bridge, *The Limestone and Dolomite Resources of the Country Around Monyash, Derbyshire: Description of 1:25000 resource sheet SK 16*, Mineral Assessment Report 26 for the Institute of Geological Sciences, Her Majesty's Stationary Office, London, 1977; (b) P. Shand, W. M. Edmunds, A. R. Lawrence, P. L. Smedley, S. Burke, *The Natural (Baseline) Quality of Groundwater in England and Wales*, Environment Agency Technical Report NC/99/74/24, Groundwater Programme Research Report RR/07/06, British Geological Survey, Keyworth, 2007.
34. W. M. Edmunds, J. M. Cook, W. G. Darling, D. G. Kinniburgh, D. L. Miles, A. H. Bath, M. Morgan-Jones, J. N. Andrews, Baseline geochemical conditions in the Chalk aquifer, Berkshire, U.K.: a basis for groundwater quality management, *Appl. Geochem.*, 1987, **2**, 251.
35. W. R. Jones, *Minerals in Industry*, 3rd edn., Penguin, London, 1955.
36. A full range of chalk-derived lime products quarried and manufactured by Singleton Birch, Ltd., together with their physico-chemical characteristics, is available on their website: http://www.singletonbirch.co.uk (accessed December 28, 2021).
37. Thermal oxidation of rhodochrosite at kiln temperatures affords hausmannite: (a) L. Biernacki, S. Pokrzywnicki, The thermal decomposition of manganese carbonate: thermogravimetry and exoemission of electrons, *J. Thermal Anal. Calorim.*, 1999, **5**, 227; both bixbyite and pyrolusite likewise decompose to hausmannite under thermal kiln conditions: (b) E. Alonso, C. Hutter, M. Romero, A. Steinfeld, J. Gonzalez-Aguilar, Kinetics of Mn_2O_3-Mn_3O_4 and Mn_3O_4-MnO redox reactions performed under concentrated thermal radiative flux, *Energy Fuels*, 2013, **27**, 4884; (c) N. Birkner, A. Navrotsky, Thermodynamics of manganese oxides: effects of particle size and hydration on oxidation-reduction equilibria among hausmannite, bixbyite and pyrolusite, *Am. Mineralogist*, 2015, **97**, 1291; the whole picture is further complicated by phase transformations: (d) A. N. Grundy, B. Hallstedt, L. J. Gauckler, Assessment of the Mn-O system, *J. Phase Equilib.*, 2003, **24**, 21.
38. Oxidation of iron pyrite at kiln temperatures affords the sesquioxide: (a) G.-M. Schwab, J. Philinis, Reactions of iron pyrite: its thermal decomposition, reduction by hydrogen and air oxidation, *J. Am. Chem. Soc.*, 1947, 69, 2588; (b) T. Kennedy, B. T. Sturman, The oxidation of iron(II) sulphide*, J. Thermal Anal.*, 1975, 8, 329; (c) Y. Zhang, Q. Li, X. Liu, B. Xu, Y. Yang, T. Jiang, A thermodynamic analysis on the roasting of pyrite, *Minerals*, 2019, 9, 220; likewise, oxidation of siderite proceeds to magnetite: (d) B. M. French, P. E. Rosenberg, Siderite ($FeCO_3$): thermal decomposition in equilibrium with graphite, *Science*, 1965, 147, 1283; and then maghemite: (e) M. Aliahmad, N. N. Moghaddam, Synthesis of maghemite (γ-Fe_2O_3) nanoparticles by thermal decomposition of magnetite (Fe_3O_4) nanoparticles, *Mater. Sci. Poland*, 2013, 31, 264; (f) Note that the kiln conditions are controlled to ensure sufficient fugacity of oxygen, in a manner similar to those in the Earth: see, for example, V. Stagno, S. Aulbach, Redox processes before, during, and after Earth's accretion affecting the deep carbon cycle, in R. Moretti, D. R. Neuville (eds.), *Magma Redox Geochemistry*, Wiley, Hoboken, NJ, 2022, p.21.
39. (a) D. S. McClure, The distribution of transition metal cations in spinels, *J. Phys. Chem. Solids*, 1957, **3**, 311; (b) J. D. Dunitz, L. E. Orgel, Electronic properties of transition metal oxides II: cation distribution amongst octahedral and tetrahedral sites, *J. Phys. Chem. Solids*, 1957, **3**, 318; (c) A. H. Eschenfelder, Ionic valences in manganese-iron spinels, *J. Appl. Phys.*, 1958, **29**, 378; (d) S. K. Sahu, B. Huang, K. Lilova, B. F. Woodfield, A. Navrotsky, Thermodynamics of Fe_3O_4-Co_3O_4 and Fe_3O_4-Mn_3O_4 spinel solid solutions at the bulk and nanoscale, *Phys. Chem. Chem. Phys.*, 2015, **17**, 22286.
40. (a) A. T. Stone, J. J. Morgan, Reduction and dissolution of manganese(III) and manganese(IV) oxides by organics: 1: reaction with hydroquinone, *Environ. Sci. Technol.*, 1984, **18**, 450; (b) A. T. Stone, Reductive dissolution of manganese(III/IV) oxides by substituted phenols, *Environ. Sci. Technol.*, 1987, **21**, 979; (c) K. L. Johnson, C. M. McCann, C. E. Clarke, Breakdown of organic contaminants in soil by manganese oxides: a short review, in I. A. M. Ahmed, K. A. Hudson-Edwards (eds.), *Redox-Reactive Minerals: Properties, Reactions and Applications in Natural Systems and Clean Technologies*, EMU Notes in Mineralogy, volume 17, chapter 11, The Mineralogical Society of Great Britain and Ireland, London, 2017, p.313; (d) B. Liu, Y. Zhang, M. Lu, Z. Su, G. Li, T. Jiang, Extraction and separation of manganese and iron from ferruginous manganese ores: a review, *Mineral. Eng.*, 2019, **131**, 286; (c) V. Singh, S. Pati, K. Kumar, Development of a process to produce manganese nanomaterials from low grade ferruginous manganese ores, *Mineral Process. Extract. Metallurg.*, 2021, **130**, 324.
41. (a) S. Licht, V. Naschitz, L. Halperin, L. Lin, J. Chen, S. Ghosh, B. Liu, Analysis of ferrate(VI) compounds and super-iron Fe(VI) battery cathodes: FTIR, ICP, titimetric, XRD, UV/VIS, and electrochemical characterisation, *J. Power Sources*, 2001, **101**, 167; (b) Y. L. Wang, S. H. Ye, J. K. Bo, Y. Y. Wang, F. Wu, Electrochemical reduction mechanism of Fe(VI) at a porus Pt black electrode, *J. Electrochem. Soc.*, 2009, **156**, A572; (c) S. Barışçı, F. Ulu, H. Särkkä, A. Dimoglo, M. Sillanpää, Electrosynthesis of ferrate(VI) ion using high purity iron electrodes: optimisation of influencing parameters on the process and investigating its stability, *Int. J.*

Electrochem. Sci., 2014, **9**, 3099; (d) Y.-L. Wei, Y.-S. Wang, C.-H. Liu, Preparation of potassium ferrate from spent steel pickling liquid, *Metals*, 2015, **5**, 1770; (e) J.-Q. Jiang, C. Stanford, M. Petri, Practical application of ferrate(VI) for water and wastewater treatment – site study approach, *Water-Energy Nexus*, 2018, **1**, 42; (f) B. Shao, H. Dong, X. Guan, Rôle of ferrate(IV) and ferrate(V) in activating ferrate(VI) by calcium sulphite for enhanced oxidation of organic contaminants, *Environ. Sci. Technol.*, 2019, **53**, 894; (g) P. C. W. Cheung, D. R. Williams, J. Barrett, J. Barker, D. W. Kirk, On the origins of some spectroscopic properties of "purple iron" (the tetroxoferrate(VI) ion and its Pourbaix safe-space, *Molecules*, 2021, **26**, 5266; (h) Note that calcium ions can catalyse the decomposition of ferrate: L. Ma, W. W. Y. Lam, P.-K. Lo, K.-C. Lau, T.-C. Lau, *Angew. Chem. Int. Edn.*, 2016, **55**, 3012.

42. See, for example, S. G. Simpson, The effect of the presence of filter paper on permanganate-oxalate titrations, *J. Ind. Eng. Chem.*, 1921, **13**, 1152
43. (a) B. E. Dixon, J. L. White, The reaction between manganese salts and sodium hypochlorite in the presence of certain other salts, *J. Chem. Soc.*, 1927, 1469; (b) M. Valensi, Nouvelle méthode d'enseignement de la chimie minérale, *Bull. Union des Physiciens*, No. 394, 1950, 61; (c) M. Pourbaix (ed.), *Atlas of Electrochemical Equlibria in Aqueous Solutions*, 2nd edn., National Association of Corrosion Engineers, Houston, Texas, 1974.
44. K. M. Love, A. Woronow, Chemical changes induced in aragonite using treatments for the destruction of organic material, *Chem. Geol.*, 1991, **93**, 291.
45. (a) W. M. Latimer, *The Oxidation States of the Elements and their Potentials in Aqueous Solutions*, 2nd edn., Prentice-Hall, New York, 1952; (b) K. Ishikawa, T. Yoshioka, T. Sato, A. Okuwaki, Solubility of hæmatite in LiOH, NaOH and KOH solutions, *Hydrometallurgy*, 1997, **45**, 129; (c) S. Uchida, T. Sato, A. Okuwaki, Formation of Na_xFeO_2 by the oxidation of iron powder in concentrated sodium hydroxide solutions at elevated temperatures, *J. Mater. Sci.*, 1995, **14**, 633.
46. (a) See, for example, B. M. Voelker, D. L. Sedlak, Iron reduction by photo-produced superoxide in seawater, *Marine Chem.*, 1995, **50**, 93; (b) S. Garg, G. Xing, T. D. Waite, Influence of pH on the kinetics and mechanism of photo-reductive dissolution of amorphous iron oxyhydroxide in the presence of natural organic matter: implications to iron bioavailability in surface waters, *Environ. Sci. Technol.*, 2020, **54**, 6771.
47. See, for example, (a) H. P. Hopkins, Jr., C. A. Wulff, The solution thermochemistry of polyvalent electrolytes: I: calcium hydroxide, *J. Phys. Chem.*, 1965, **69**, 6; (b) W. B. Euler, L. J. Kirschenbaum, B. Ruekberg, Determination of K_{sp}, ΔG^0, ΔH^0 and ΔS^0, *J. Chem. Educ.*, 2000, **77**, 1039.
48. (a) J. R. Lewis, The catalytic decomposition of sodium hypochlorite solutions I: mechanism of the reaction, *J. Phys. Chem.*, 1928, **22**, 243; (b) M. W. Lister, Decomposition of sodium hypochlorite: the uncatalysed reaction, *Can. J. Chem.*, 1956, **34**, 465.
49. J. H. Atherton, Mechanism in two-phase reaction systems: coupled mass transfer and chemical reaction, in R. G. Compton, G. Hancock (eds.), *Research in Chemical Kinetics*, volume 2, Elsevier, Amsterdam, 1994, p.193.
50. As an aside, we note that whilst calcite dissolution is typically controlled by surface kinetics – see R. G. Compton, P. R. Unwin, The dissolution of calcite in aqueous solution at pH < 4: kinetics and mechanism, *Phil. Trans. R. Soc. London A*, 1990, **330**, 1, and R. G. Compton, K. L. Pritchard, The dissolution of calcite at pH > 7: kinetics and mechanism, *ibid.*, 1990, **330**, 47; acidic dissolution of calcium carbonate from Southern Province Chalk has been shown to be mass transport controlled – see R. G. Compton, C. T. Walker, P. R. Unwin, W. A. House, Dissolution kinetics of Carrera Marble, Portland Stone and several limestones in acidic waters, *J. Chem. Soc.*, *Faraday Trans.*, 1990, **86**, 849, and that different species of coccolith hold different masses of calcium carbonate *q.v.* M. Yang, C. Batchelor-McAuley, S. Barton, R. E. M. Rickaby, H. A. Bouman, R. G. Compton, Opto-electrochemical dissolution reveals coccolith calcium carbonate content, *Angew. Chem. Intl. Edn.*, 2021, **60**, 20999.
51. (a) E. M. Logothetis, K. Park, The electrical conductivity of Mn_3O_4, *Solid State Commun.*, 1975, **16**, 909; (b) R. Metselaar, R. E. van Tol, P. Piercy, The electrical conductivity and thermoelectric power of Mn_3O_4 at high temperatures, *J. Solid State Chem.*, 1981, **38**, 335; (c) S. E. Dorris, T. O. Mason, Electrical properties and cation valencies in Mn_3O_4, *J. Am. Ceramic Soc.*, 1988, **71**, 379; (d) H. Dhaouadi, A. Madani, F. Touati, *Mater. Lett.*, 2010, **64**, 2395; (e) V. C. Bose, K. Maniammal, G. Madhu, C. L. Veenas, A. S. A. Raj, V. Biju, *IOP Conf. Ser.: Mater. Sci. Eng.*, 2015, **73**, 012084.
52. J.-K. Wu, Kinetics of the reduction of hypochlorite ion, *J. Electrochem. Soc.*, 1987, **134**, 1462.
53. (a) A. Wilczak, W. R. Knocke, R. E. Hubel, M. E. Aieta, Manganese control during ozonation of water containing organic compounds, *J. Am. Water Works Assoc.*, 1993, **85**, 98; (b) W. Li, S. T. Oyama, Mechanism of ozone decomposition on a manganese oxide catalyst: 2: steady-state and transient kinetic studies, *J. Am. Chem. Soc.*, 1998, **120**, 9047; (c) J. A. Roth, D. E. Sullivan, Solubility of ozone in water, *Ind. Eng. Chem. Fundam.*, 1981, **20**, 137.
54. (a) N. S. Lawrence, B. Schöllhorn, J. D. Wadhawan, Asymmetric and anharmonic electrode kinetics: evaluation of a model for electron transfer with concerted rupture of weak, inner-shell interactions, *ChemistrySelect*, 2021, **6**, 13331; (b) B. Gilbert, G. A. Waychunas, The timescale

of mineral redox reactions, in I. A. M. Ahmed, K. A. Hudson-Edwards (eds.), *Redox-Reactive Minerals: Properties, Reactions and Applications in Natural Systems and Clean* Technologies, EMU Notes in Mineralogy, volume 17, chapter 4, The Mineralogical Society of Great Britain and Ireland, London, 2017, p. 55.; (c) M. Sander, T. B. Hofstetter, C. A. Gorski, Electrochemical analyses of redox-active iron minerals: a review of non-mediated and mediated approaches, *Environ. Sci. Technol.*, 2015, **49**, 5862.

55. A. Lu, Y. Li, F. Liu, Y. Liu, H. Ye, Z. Zhuang, Y. Li, H. Ding, C. Wang, The photo-geochemical cycle of Mn oxides on the Earth's surface, *J. Mineral. Soc.*, 2021, **85**, 22;
56. S. Fraley, Manganese levels in limestone: operational issues in wet limestone flue gas scrubbing technologies, in M. L. Thomson, J. H. Brisch (eds.), *Lime: Building on the 100-Year Legacy of the ASTM Committee C07*, Specialist Technical Publication volume 1557, American Society for Testing and Materials, San Diego, 2012, p. 167.
57. L. Lv, J. Yang, Z. Shen, Y. Zhou, J. Lu, Optimising the characteristics of calcium sulfate dehydrate in the flue gas desulfurisation process: investigation of the impurities in slurry: Cl^-, Fe^{3+} and Mn^{2+}, *Chem. Ind. Chem. Eng. Quart.*, 2017, **23**, 293.

Empowering Clean Water whilst Safeguarding Water Distribution Pipeline Integrity: Towards Manganese- and Iron-Free Lime Hydrate for Water Treatment

Dávid Kocsis,[*1,2,3] Rhys A. Ward,[2,3] Christopher R. Meyer,[*1]
Michael Thompson,[4] Timothy J. Prior,[4] Stephen M. Kelly,[3,4]
Nathan S. Lawrence,[2,3] Jay D. Wadhawan[*2,3]

[1]*Singleton Birch, Ltd., Melton Ross Quarries,*
Barnetby DN38 6AE, North Lincolnshire, United Kingdom.

[2]*Department of Chemical Engineering, The University of Hull,*
Cottingham Road, Kingston-upon-Hull HU6 7RX, United Kingdom.

[3]*Aura Innovation Centre, Bridgehead Business Park,*
Meadow Road, Hessle HU13 0GD, United Kingdom.

[4]*Department of Chemistry, The University of Hull,*
Cottingham Road, Kingston-upon-Hull HU6 7RX, United Kingdom.

[*]Corresponding authors:
E.mail: dkocsis@singletonbirch.co.uk (DK); cmeyer@singletonbirch.co.uk (CRM); j.wadhawan@hull.ac.uk (JDW)

Electronic Supplementary Information (ESI)

ESI1: Chalk and Limestone

Limestones are rocks containing essentially calcium carbonate.[S1] These can be formed through precipitation from water, usually in widespread but shallow seas (non-clastic, chemical or inorganic limestone), through the secretions or capture by aquatic organisms such as coral or microorganisms (biogenic limestone),[S2] or through the shells of dead sea creatures such as coccolithophores or foraminifera (bioclastic limestone – the grains and clasts are fossils which do not interlock, but rather are agglomerated and cemented in an ooze).[S3] Limestones often contain impurities such as clay and sands. In the United Kingdom, there are four common types of limestone: chalk, Carboniferous Limestone, oolitic limestone and magnesian limestone (dolomite, $CaCO_3.MgCO_3$).[S4] The members of the British Lime Association – the national trade organisation for industrial lime producers, use limestones quarried from either Carboniferous Limestone (Lhoist UK and Tarmac Buxton Lime) in the Peak District, or Cretaceous Chalk (Singleton Birch, Ltd.) in Humberside. We consider both limestones in turn.

Cretaceous Chalk is a friable limestone.[S5] This rock, extracted at the Melton Ross Quarries by Singleton Birch, Ltd. (with an output of over 1.5 MTe/yr),[S6] is of the Welton Formation.[S7] The Chalk, formed through the deposition of the planktonic algæ (such as *Haptophyta*),[S8] is micritic (<1% allochemical rock), and is classified as being of the Northern Province.[S9] This rock is significantly stronger, more dense and contains less moisture (moisture content is 8-10% for the Welton Formation)[S7] than that of the Southern Province,[S9,S10-S12] owing to the twin occurrence of pressure solution effects (cementing due to dissolution and re-precipitation reactions),[S13] and folding (pressure release) during the Alpine uplift.[S10,S14] Northern Province Chalk, which has greater faunal affinities with those of Germany, Poland and Russia, compared with the Chalk of the Anglo-Paris Basin,[S10,S15] was deposited in a deeper-water environment than for the Southern Province Chalk[S10,S16] – the nodular chalks and flint horizons are only weakly developed, and glauconitised and phosphatised hard-grounds are much less well-developed in Northern Province Chalk.[S16] This enables Northern Province Chalk to be used as a building stone, in for, example, Louth Park Abbey almost 900 years ago.[S17] The Chalk is characterised by calcitic particles (coccoliths in the size range of 0.5 – 4 μm within a matrix of larger, polygonal calcite crystals),[S12] with high porosity (*ca.* 22% for the Welton Formation),[S18] and, owing to it being more brittle than the Southern Province Chalk, is of high permeability (~0.01 – 10 m/day), through clean fractures.[S18]

The Chalk at Melton Ross Quarries has been reported as being extremely pure, containing 99% $CaCO_3$,[S5,S7] with flints (chert) that are, for the most part of the succession, rare.[S7] Detailed stratigraphy have been reported.[S7,S10] Certain flint bands are prominent, such as the semi-tabular, pink, Ferruginious Flint, which contains pyrite-coated fractures that have been oxidised to limonite or hæmatite.[S7] A variety of marl bands (argillaceous rocks) are dispersed throughout the formation.[S7,S10] Although the Welton Chalk is softer than the overlying

Burnham Chalk, it is still indurated, with both a lateral and vertical variation in this hardness.[S10] Accordingly, Chalk is currently blasted from the outcrop from *ca.* 2 m above the Ferruginious Flint to between the Barton Marls 2 and 1, having previously been taken from deeper lithographies (from about 3 m above the Croxton Marl to about 2 m above the organic matter derived Black Band). As demonstrated in Electronic Supplementary Information ESI5, X-ray powder diffraction of a sample from the current quarry face confirms that the only crystalline phase present is calcite. Digestive analysis through ICP-OES (see Electronic Supplementary Information ESI4) revealed that the manganese level in chalk derived from the current quarry face is 30 mg/kg less than that from the deeper Welton Chalk lithographies previously quarried.

The Bee Low Limestone in Derbyshire is quarried by two UK lime manufacturers: Lhoist and Tarmac. This Carboniferous formation forms around 90% of the limestone outcrop in this area, and is of considerable economic importance.[S19,S20] The pale grey, limestone beds were deposited in an open-marine shelf environment, and are chert-free: they are typically lithographically uniform.[S19,S20] However, several clay bands (red-brown to green-grey), typically 0.5 m thick, are dispersed within the formation, thought to originate from the wide-spread, but intermittent falling of volcanic ash – volcanism was most active in the later part of the Dinantian.[S20] Nevertheless, the limestone is considered to be very high purity (CaO content is between 52.40 – 56.18 wt.%, with a mean of 55.41 ± 0.83 wt.%), with small impurities due to iron (Fe_2O_3 is reported to range between 70 – 31100 ppm, with a mean of 713 ± 2973 ppm) and manganese (MnO ranges between 40 – 700 ppm, with a mean of 119 ± 93 ppm).[S19,S20]

ESI2: Redox Boundaries in Groundwater Geochemistry

The redox potential (E_h, open-circuit potential *vs.* the Standard Hydrogen Electrode) of groundwater is an important parameter that marks its quality (chemical composition).[S21] For iron and manganese, this parameter is crucial as oxidised and reduced states have different (pH-dependent) aqueous solubilities. As an optimised parameter, however, E_h, which is measured as the potential of a platinum electrode with respect to a reference, is plagued by instabilities and experimental difficulties, since (1) the platinum surface can be fouled by both oxygen (forming platinum oxides) and hydroden sulfide (forming platinum sulfides), leading to inaccurate measurements under both oxic and anoxic conditions; (2) reactions can occur at the liquid junction of the reference electrode (including precipitation of heavy metal sulfides), causing measurement drift; and (3) the occurrence of mixed potentials during operations can give rise to poor reproducibility in measurements. Indeed, Whitfield[S22] has suggested that in the oxygenated environment of an unconfined aquifer, platinum electrodes behave as platinum oxide electrodes and respond to pH; in a confined aquifer environment, where H_2S is present, the slow formation of platinum sulfides pushes the value of E_h to more negative potentials. Nevertheless, E_h continues to be used as a convenient operational parameter to monitor changes in the redox system in flowing groundwater, as it is considered to provide an indication of the redox states of the water.[S23]

Manganese and iron ions are both redox active in bicarbonate-rich water at pH between[S24] 6.75 and 7.75. Under these conditions, divalent manganese (Mn^{2+}) and iron (Fe^{2+}) are soluble in water, but tetravalent manganese (MnO_2) and trivalent iron (FeOOH and $Fe(OH)_3$) are not. In the (Northern Province) Chalk aquifer of the East Riding of Yorkshire, for example, there is a small difference of *ca.* 300 mV in groundwater E_h on either side the former cliff-line buried in the Eemian (Ipswichian interglacial).[S25] This difference in redox potential (redox boundary) coincides with a change in dissolved oxygen (from >10 ppm to <4 ppm), and enables the hydrogeochemical mapping of the unconfined, semi-confined and confined aquifers.[S16,S25] Indeed, in the confined aquifer, Mn^{2+} and Fe^{2+} have been quantified at levels of as much as 100 and 1000 ppb, respectively, whilst in the unconfined and semi-confined aquifers, Mn^{2+} and Fe^{2+} have been measured to have levels below 20 and 50 ppb, respectively.[S16,S25]

A similar picture has been found in the (Southern Province) Chalk aquifer of the Anglo-Paris Basin:[S26] E_h values in the range 330-420 mV are associated with the unconfined aquifer, where dissolved oxygen levels are typically between 8-10 mg/L; these drop sharply to <160 mV with the complete disappearance of oxygen in the confined aquifer, which marks the redox boundary.[S26] It follows that such redox boundaries not only mark the changes in hydrogeochemistry, but also in the *chemistry of the trace redox elements in the aquifer rocks*.

ESI3: The Lime Cycle

The lime cycle refers to the process of mining calcium carbonate ($CaCO_3$), calcining this at temperatures up to 1100 ^{o}C to form quicklime (CaO), followed by hydration with water to yield slaked lime ($Ca(OH)_2$), which can be re-carbonated to $CaCO_3$ using carbon dioxide.[S27] As indicated in the Abstract of the main paper, the lime cycle is also used for dolomites.

At the Melton Ross Quarries, Singelton Birch, Ltd. manufacture slaked lime from quarried rock through the following typical manufacturing operations.

1. Limestone is blasted from the quarry face, to yield blocks typically in excess of 2 m. Unlike other limestones, the rock cannot be washed and cleaned with water, since the chalk is too friable.
2. The blocks are hauled into the primary crusher, which produces smaller stones (<200 mm in size) and fines. These are conveyed to the quarry fines plant, where very fine dust (< 5mm) is removed and supplied for use, whilst the remaining rocks are further conveyed to the stone blending plant, where they are separated by size into large (*ca.* 180 – 80 mm), medium (*ca.* 80 – 50 mm) and small (down to *ca.* 2 in). Small and medium stones are sorted optically, whilst the larger stones pass through X-ray sorting. These then pass through to the 180 Te storage hoppers, before waiting to enter the kiln in turn.
3. The sorted carbonate stones are fed, batch-wise, into the tops of highly efficient, gas-fired, vertical, Maerz PFR kilns, where they are calcined to afford calcium oxide. The top part of the kiln acts as a pre-heating zone, and is above the burning zone where the gas lances are located. As material falls below the gas lances, cold air is blown to cool the lime product. The kilns are fitted with a venturi scrubber, so as to remove any reactive lime particles from the flue gases, whilst at the same time abating both SO_2 (from the natural gas used) and CO_2 (from both gas combustion and carbonate decomposition) from the exhaust.
4. The produced lime (Burnt Lime 40) passes first to storage, and then is crushed and screened using a vibrating plate.
5. The majority of the screened lime is progressed to the hydrators, where reaction with a water spray takes place, to furnish the slaked lime product.
6. The oversize lime from the screen, if the quality is sufficiently high, is sent to the microlime plant, where the lime is further crushed to yield micron-sized lime (microlime 90), or processed through air classification to yield two lime products: one with size ≤ 45 μm and the rest (microlime 10-90).
7. Products are assessed for quality compliance, for example through analysis of the silica content, loss-on-ignition, *etc.*, and packed for storage, shipping and onward operations.

ESI4: Experimental Methods

Chemical Reagents

All manufactured samples of $CaCO_3$, CaO and $Ca(OH)_2$ were used, as received, from Singleton Birch, Ltd. This included a sample of lime hydrate derived from Carboniferous Limestone. The chalk, screenings and chalk-derived lime hydrate used were processed at the Melton Ross Quarries, from Cretaceous Chalk derived from both the middle stratitographic section (between the Melton Ross Marl and the Barton Marl 1) and the bottom bed (between the Grasby Marl, to just below the Chalk Hill Marl, but above the organic Black Band) of the Melton Ross Quarries. All other chemical reagents used were supplied by Fisher Scientific (aklaine sodium hypochlorite solution, laboratory grade), or Sigma-Adrich, with magnetite and maghæmite generously supplied by ParagonID, Ltd. Doubly deionised and filtered water, with a resistivity greater than 18 MΩ cm was taken from an Elgastat system (Vivendi). Oxygen and nitrogen were supplied by Air Products. Ozone was generated from a pure oxygen supply using an ozone generator (LAM2, Suez Water Technologies & Solutions).

Chemical Etching Methods

Unless otherwise specified, all experiments were undertaken under ambient temperature conditions (20 ± 2 ^{o}C). Chemical etching experiments were undertaken in triplicate, typically involved a 1 g of lime hydrate and 80 mL (100 g) of alkaline hypochlorite solution (8% or 14%), either in an open beaker under quiescent conditions (or stirred with a magnetic flea), or in a round-bottomed flask equipped with a Liebig condenser and refluxed at 90 ^{o}C for a fixed time period, in a fume cupboard. Ozone etching was undertaken under ambient temperature, using a similar volume of water as in the hypochlorite experiments, with continued bubbling of ozone in a stirred aqueous $Ca(OH)_2$ slurry for a specified length of time, in a fume cupboard. In both cases, pink supernatants were observed, which were removed through either vacuum filtration or centrifugation for spectrophotometric analysis. In the former case, the resulting filter cake was dried in an oven at 110 ^{o}C, and the upper part analysed *via* inductively coupled plasma-optical emission spectrometry (ICP-OES). For vacuum filtration, ceramic filters were preferred, since when paper-based filters were used, the filtrate changed colour[S28] from pink to blue and green, and then to yield a colourless solution! This could be due to the reduction of pink permanganate (MnO_4^-) to unstable blue hypomanganate (MnO_4^{3-}),[S29] and then to green manganate (MnO_4^{2-}), and ultimately yielding solid brown manganese dioxide (MnO_2), with the red ferrate ion (FeO_4^{2-}) being reduced to yellow ferric hydroxide ($Fe(OH)_3$), presumably by sulfite-derivatised celluloid fibres in the paper filter, formed during the paper pulping process.[S30] In the case of experimental cascade etches, the dried filter cake was used as the feed for each subsequent etch, with each feed appearing increasingly more "white".

For the case of experiments using calcite with gœthite (ironstone), the raw ironstone sample, generously supplied by Johnston Quarry Group, was broken up, and ground using an agate pestle and mortar. 1.0 g of this sample was refluxed with 80 mL of alkaline hypochlorite (14%) at 90 ^{o}C for 1 hr. The absence of a pink or red coloration was noted.

ICP-OES Analysis

Chalk, lime and lime hydrate contain silicate-based impurities. Accordingly, solid samples were first digested in HF: solid samples were weighed to four decimal place and transferred into PTFE digestion vessels. Sample size ranged typically from 0.1 - 0.5 g. A solution of 3 mL of concentrated nitric acid, 1 mL of concentrated hydrochloric acid (*i.e.* aqua regia) and 1 mL of 40% hydrofluoric acid were also added to each digestion vessel, to dissolve any silica present in the solid sample. All acids used were Romil super-purity spectroscopic grade. The digestion vessels were then closed and inserted into a carousel, which was then placed in a CEM Mars 5 microwave-assisted digester. Following a pre-set programme the vessel temperature was heated to 200 °C over a 15 min period, then was held constant at this temperature for a further 20 min. The temperature of the solution and pressures within digestion vessel were constantly measured in real time within the No 1 or control vessel. Pressures of 200 – 250 psi are typical at the higher temperatures. After cooling, each vessel was opened and 4mL of 4% spectroscopic grade boric acid was injected. The vessels were then placed back into the microwave and heated again to 170 °C in 15 min, and held at this temperature for 15 min. The addition of the boric acid “mops up” any remaining HF by forming BF_4^-. This second stage is required because samples containing free HF cannot be introduced into the ICP due to its internal glass components. After cooling again, the digests were then transferred to tared Sarstedt tubes. The digestion vessels were rinsed three times with ultra high quality (UHQ) water, the washings added to the tubes and the whole solution made up to 40 mL with UHQ water. The tubes were then weighed to four decimal places giving the weight of the digest, followed by their analysis for their iron and manganese contents by ICP-OES. The instrument used was a Perkin Elmer Optima 5300 DV, and each run was calibrated using Romil certified Standards.

Iron and manganese levels in the original solid samples were then calculated using the measured levels within the digest, the digest weight and the original sample weight.

Visible Spectroscopy

Visible spectroscopy of the pink supernatant was undertaken using a PerkinElmer Lambda-25-Scan-UV–Vis instrument, using a quartz cell of 1.0 cm path length.

X-Ray Powder Diffraction

Samples of chalk and lime hydrate derived from chalk were examined by X-ray powder diffraction performed on a PANAlytical Empyrean X-ray diffractometer (XRD) operating in

Bragg-Brentano geometry using copper $K\alpha_1$ radiation (λ = 1.54056 Å), and a PIXEL detector. Patterns were fitted and the phases present identified using the PDF2 database.[S31]

The pattern for the lime hydrate sample was fitted using Rietveld refinement[S32] to obtain a quantitative assessment of the amount of each crystalline phase present. The background was fitted using a nine-term shifted Chebyshev polynomial. Peaks were fitted using a pseudo-Voigt peak shape. For each phase, lattice parameters and profile parameters were refined. A single zero-point correction was refined. Preferred orientation in the portlandite phase was treated using standard methods.

ESI5: X-Ray Diffraction Studies of Chalk and Lime Hydrate

The X-ray powder diffraction pattern of chalk taken from the Melton Ross Quarries is shown in Figure S1. This confirms that the only crystalline phase present is calcite, which is highly crystalline.

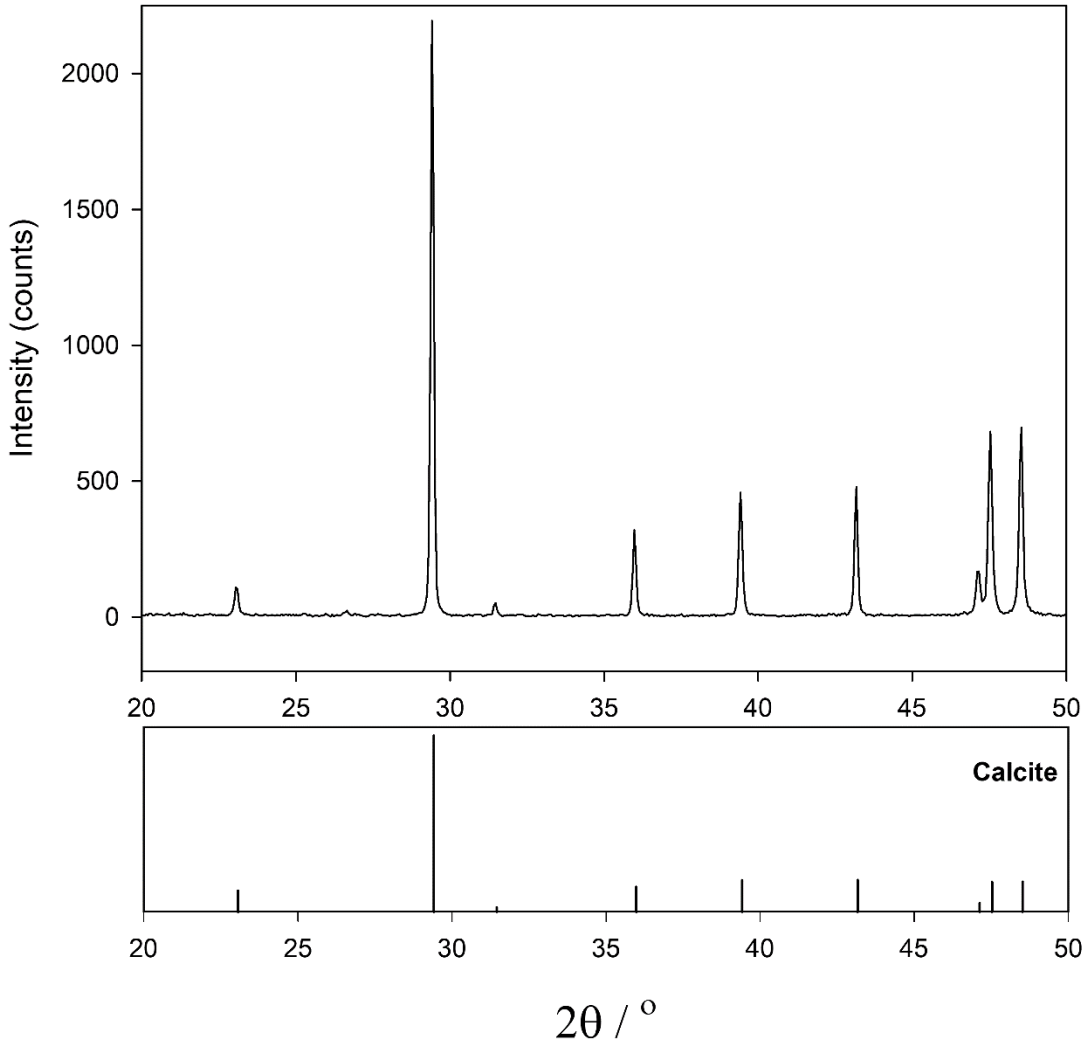

Figure S1: *X-Ray powder diffraction pattern of chalk. The lower panel shows the allowed peak positions for calcite and the relative peak intensities. The sample was of Welton formation Chalk derived from screenings obtained from the middle stratitographic section (between the Melton Ross Marl and the Barton Marl 1).*

The X-ray powder diffraction pattern of lime hydrate is shown in Figure S2. This sample contains two crystalline phases; the dominant phase is portlandite and there is a smaller amount of highly crystalline calcite. It was possible to fit the observed data using the Rietveld method and a good fit was obtained (R_p = 5.63 %). This revealed the sample contained portlandite and calcite in the ratio 97.2 : 2.8 ± 0.2 % by weight.

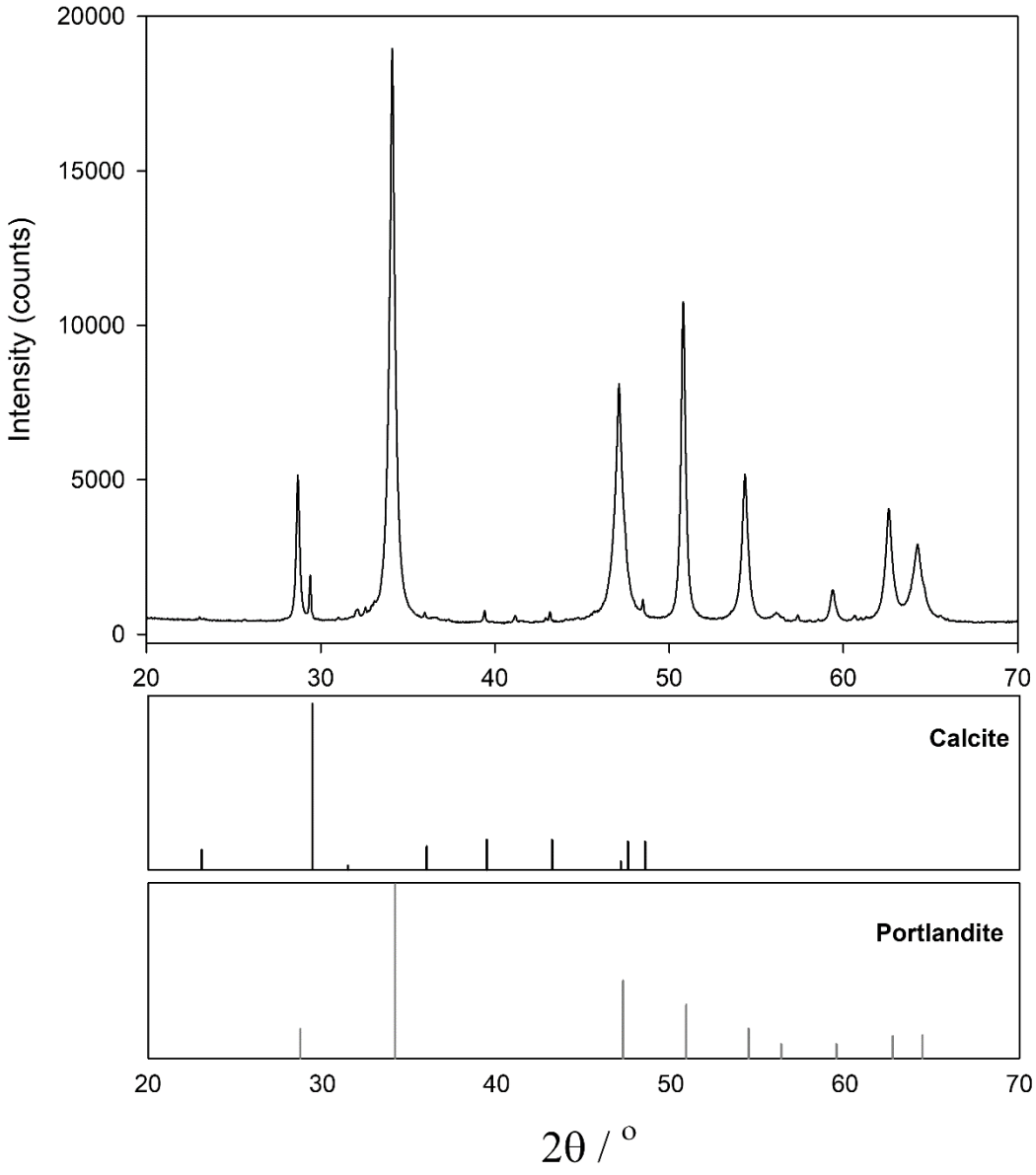

Figure S2: *X-Ray powder diffraction pattern of lime hydrate derived from Welton formation Chalk screenings obtained from the middle stratitographic section (between the Melton Ross Marl and the Barton Marl 1). The lower panels show the allowed positions and relative intensities of peaks for calcite and portlandite.*

Note that the ratio of portlandite to calcite was estimated through performing a routine two-phase Rietveld refinement, using GSAS implemented within EXP-GUI. The portlandite phase is well known to suffer from preferred orientation and this was treated using standard methods in GSAS employing spherical harmonics.[S33] The fit is less than ideal because of this effect but the fit indicators are reasonable: wR_p = 0.0895 and R_p = 0.0563. The fit to the observed data is shown in Figure S3.

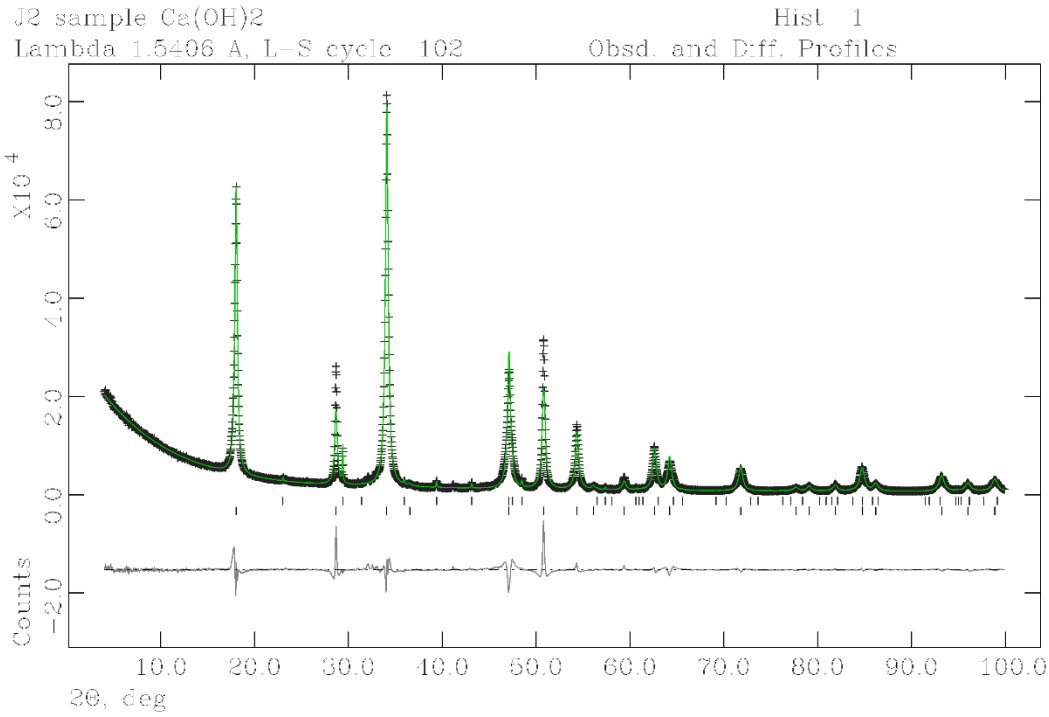

Figure S3: *X-Ray diffraction profiles for lime hydrate derived from Welton formation Chalk screenings obtained from the middle stratitographic section (between the Melton Ross Marl and the Barton Marl 1). Raw data are shown as black crosses; green line is the calculated pattern; the lower solid line is the difference plot. The upper tick marks represent allowed peak positions for calcite and the lower tick marks represent allowed peak positions for portlandite.*

ESI6: Spectroscopic Evidence of MnO_4^- and FeO_4^{2-}

Figure S4 illustrates the visible spectrum of the pink supernatant obtained on incubating lime hydrate with alkaline hypochlorite at under ambient conditions for 72 hr. The split-peak at *ca.* 520 nm fingerprints the permanganate (MnO_4^-) anion, with the two further peaks at *ca.* 495 nm, and 540 nm, which match-up with that expected from ferrate (FeO_4^{2-}).[S34]

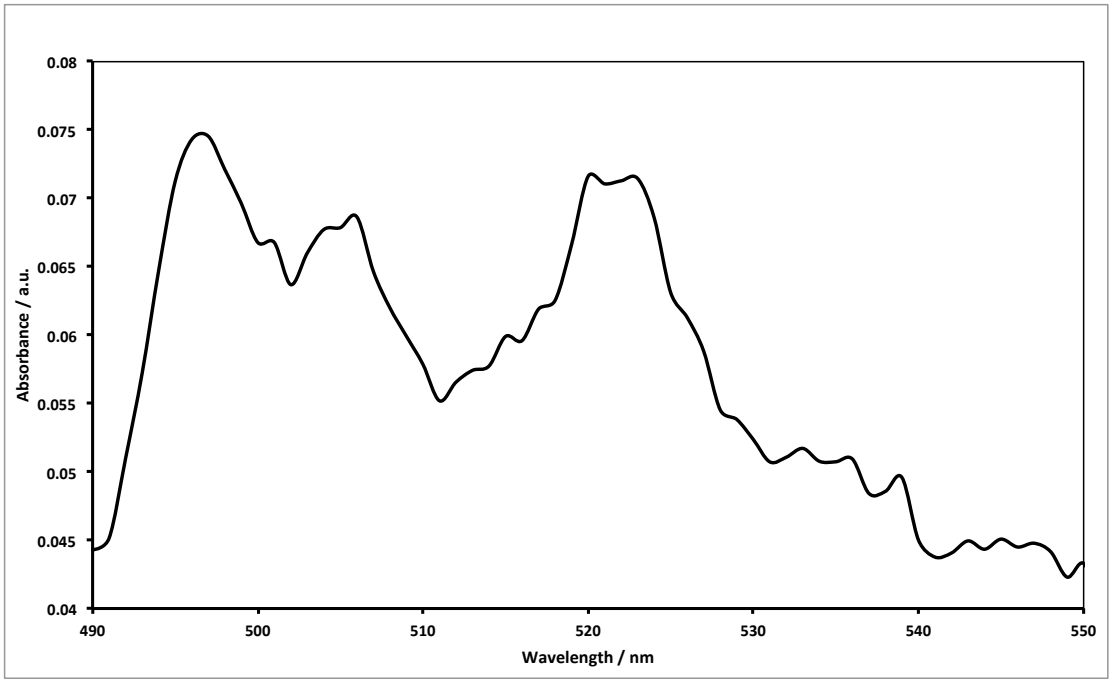

Figure S4: *Spectrophotometric fingerprinting of MnO_4^- and FeO_4^{2-} present in the supernatant following incubation of lime hydrate derived from Welton formation Chalk screenings obtained from the middle stratitographic section (between the Melton Ross Marl and the Barton Marl 1), with alkaline hypochlorite.*

ESI7: Experiments with an Ironstone

A sample of Great Tew Ironstone (Great Tew, Chipping Norton, Oxfordshire, UK) was generously provided by Johnston Quarry Group. The sample was crushed in an agate pestle and mortar, and analysed by X-ray diffraction, see Figure S5.

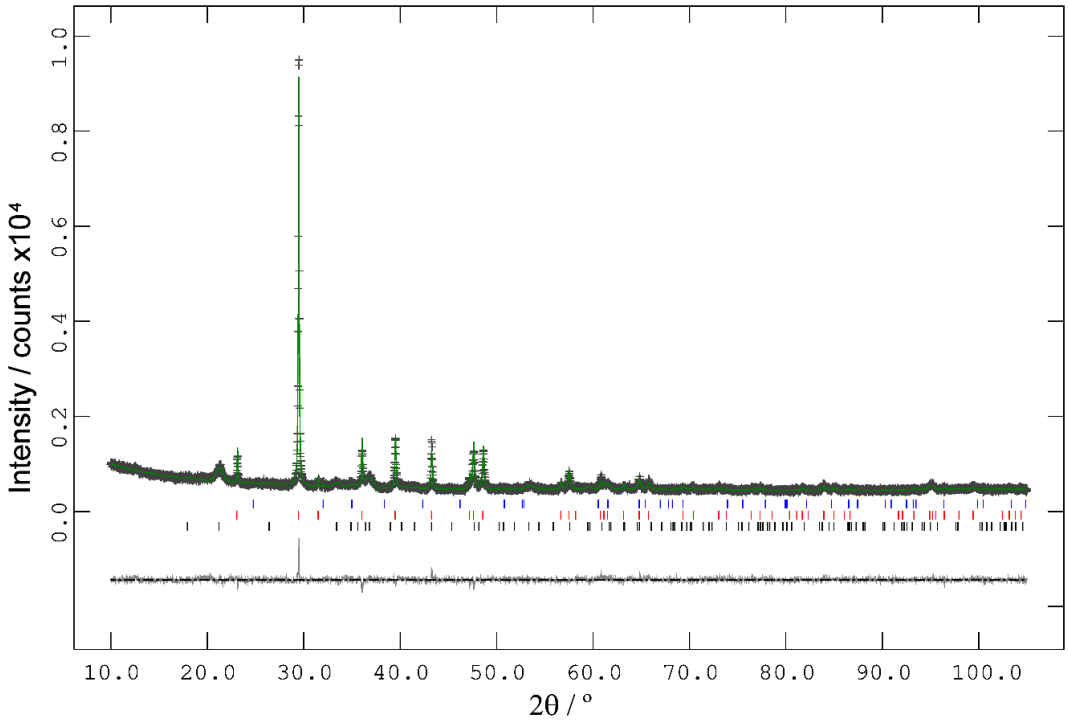

Figure S5: *X-Ray diffraction profiles for ironstone derived from Great Tew quarry. Raw data are shown as grey crosses; green line is the calculated pattern; the lower solid line is the difference plot. The upper tick marks represent allowed peak positions for siderite; middle tick marks show allowed peak positions for calcite; the lower tick marks represent allowed peak positions for gœthite.*

The X-ray powder diffraction pattern is dominated by peaks of calcite, with a smaller amount of gœthite and a trace amount of siderite. It was possible to undertake undertake quantitative analysis of the diffraction data using the Rietveld method and a good fit was obtained (R_p = 3.48 %). The composition of the sample by weight is calcite 82.4(3)%, goethite 17.2(3)%, and siderite (0.43(7)%).

The analysis is complicated by the fact that the powder diffraction pattern of siderite is dominated by a single peak vastly more intense than the others; here that peak is 100 times less intense than the strongest peak for calcite. Accordingly, a zoom-in on the low angle region helped identify the three phases (see Figure S6).

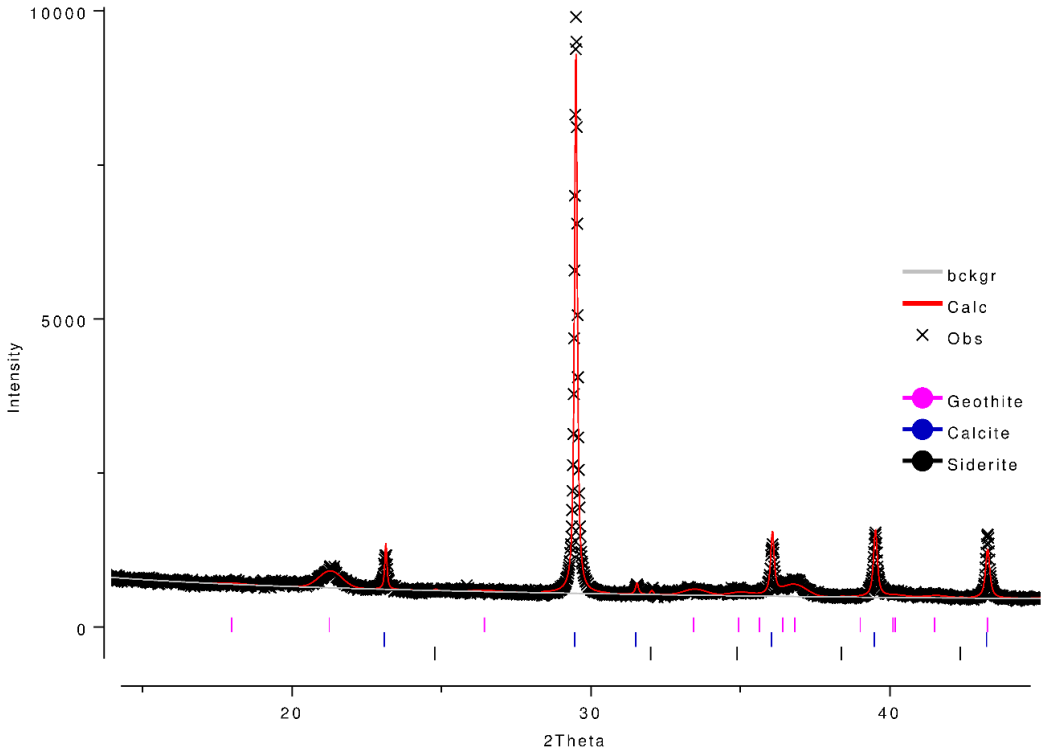

Figure S6: *X-Ray powder diffraction pattern of Great Tew Ironstone with raw data shown as black crosses in the range 15 < 2θ/° < 45. Upper tick marks show allowed peak positions of gœthite; middle ticks show allowed peak positions of calcite; lower tick marks show peak positions for siderite.*

Refined unit cell parameters for the three phases are given below.

	a / Å	**b / Å**	**c / Å**	**α / °**	**β / °**	**γ / °**	**Volume / Å^3**	**Space group**
Gœthite	9.862(4)	3.0044(12)	4.6143(18)	90	90	90	136.72(7)	*Pnma*
Calcite	4.98156(15)	4.98156(15)	17.0285(6)	90	90	120	365.96(3)	*R* -3 *c*
Siderite	4.687(2)	4.687(2)	15.417(11)	90	90	90	293.34(19)	*R* -3 *c*

Quality of fit factors (31 variables):

wRp (fitted)	Rp (fitted)	wRp (no background)	Rp (no background)	χ^2
0.0451	0.0348	0.0686	0.0491	1.147

ESI8: Retrograde Solubility of $Ca(OH)_2$ with Temperature

We consider the solubility equilibrium for calcium hydroxide in water:

$$Ca(OH)_2(s) \rightleftharpoons Ca^{2+}(aq) + 2OH^-(aq) \qquad \text{(S1)}$$

for which the solubility product is[S35] $K_{sp} = a_{Ca^{2+}}\left(a_{OH^-}\right)^2 = 4.68\times10^{-6}$ at 25 °C (yielding a solution of pH 12.3). Assuming the standard enthalpy change for this dissolution equilibrium is independent of temperature (*viz.*, $\Delta H^0 = -12.60\ kJ/mol$, based on the value calculated using standard enthalpies of formation, and validated experimentally),[S36] the van't Hoff equation, $\ln\left\{\frac{\left(K_{sp}\right)_{T=T_2}}{\left(K_{sp}\right)_{T=T_1}}\right\} = \frac{\Delta H^0}{R}\left(\frac{T_2 - T_1}{T_1 T_2}\right)$, enables the estimation of the temperature dependence of the solubility product. We find that at 20 °C, K_{sp} = 5.10 x 10^{-6}, and at 90 °C, K_{sp} = 1.88 x 10^{-6}. Assuming activity coefficients are unity, this corresponds to lime hydrate solubilities of 0.80 g/L at 20 °C, which reduces to 0.58 g/L as the temperature increases to 90 °C. This is the retrograde solubility of lime hydrate with temperature – the solubility of $Ca(OH)_2$ decreases with temperature, in agreement with experimental observations.[S36,S37]

It follows that, at the ambient temperatures used in this work (20 °C), in 80 mL of pure water, 1.0 g of pure $Ca(OH)_2$ (mole fraction ratios 0.003 : 0.997) will lose only 6.4% of its mass through dissolution; this decreases to 4.6 wt.% at 90 °C. However, these values are decreased further by the common-ion effect in the alkaline hypochlorite solutions used (alkalinity ≤ 2% by mass, density ~1.25 g/mL), where the hydroxide ion concentration is estimated as 0.6 M (recognising that sodium hydroxide solutions are hygroscopic), corresponding to pH ~ 13.8. Under these conditions, at 20 °C, the solubility of $Ca(OH)_2$ reduces to 1.1 mg/L, so that only 0.01% (by mass of $Ca(OH)_2$ would dissolve under the typical experimental conditions used. The retrograde solubility of $Ca(OH)_2$ causes this dissolutive loss to reduce to 0.003 wt.% by mass at 90 °C. This loss is essentially negligible at the experimental scale considered in this work.

ESI9: Zeroth-Order Heterogeneous Kinetics for Impurity Dissolution

The observation of zeroth-order heterogeneous kinetics results from (1) a very slow rate constant for the oxidative etching process, and (2) the large concentrations of the hypochlorite (or ozone) oxidant, as demonstrated below.

We consider the case where the manganese surface impurity of an inert solid, spherical particles (monodisperse in size) dissolves when suspended and mixed uniformly in an aqueous solution containing an oxidant (of bulk concentration c_0). The surface reaction flux (j_{int}):

$$j_{\text{int}} = k_s c_{\text{int}} \tag{S2}$$

comprises the product of the interfacial concentration of the oxidant (c_{int}) and the interfacial rate constant (k_s, given in length per unit time). This interfacial rate constant is the product of the surface coverage of the manganese impurity (as amount per unit area, Γ_{Mn}) and a "true" heterogeneous rate constant, k_s^0: $k_s = k_s^0 \Gamma_{Mn}$. The mass transport flux (j_{sol}) of chemical oxidant to the surface is given by:

$$j_{sol} = k_L \left(c_0 - c_{\text{int}} \right) \tag{S3}$$

in which k_L is the mass transfer coefficient. The flux expressions in (S2) and (S3) are equal at the interface,[S38] yielding,

$$c_{\text{int}} = \frac{k_L}{k_s + k_L} c_0 \tag{S4}$$

Since the dissolutive rate of reaction ($\frac{d[Mn]}{dt}$) is given by $\frac{d[Mn]}{dt} = -j_{\text{int}} \frac{S}{V}$, where [Mn] is the concentration of the manganese impurity in the solid, S is the total interfacial area exposed for reaction and V is the total volume of the solid particles, we find,

$$-\frac{d[Mn]}{dt} = \frac{k_s k_L}{k_s + k_L} \frac{S}{V} c_0 = \frac{3}{r_0} \frac{k_s k_L}{k_s + k_L} c_0 = \frac{3}{\sqrt[3]{\frac{3m}{4\pi N \rho}}} \frac{k_s k_L}{k_s + k_L} c_0 \tag{S5}$$

where r_0 is the radius of the inert solid particles, ρ is the density of the inert solid, m is the mass of the inert solid and N is the number of solid particles present. Thus, from equation (S5), monodispersity in the solid causes limited, if any, variation in the dissolution rate with mass of solid present. Thus, in the limit when the mass transport is faster than the surface dissolution reaction, the dissolution rate is given by,

$$-\frac{d[Mn]}{dt} \approx \frac{3}{\sqrt[3]{\frac{3m}{4\pi N \rho}}} k_s c_0 \tag{S6}$$

Since the manganese impurity is present at a trace level compared with the oxidant, all of the variables on the right-hand side of equation (S6) are effectively constant, leading to the observation of zeroth-order heterogeneous reaction kinetics. Since equation (1) in the main paper is in terms of the number moles of the manganese impurity, *viz.*, $\frac{d\left(n_{Mn}\right)_{solid}}{dt} = -k_{het}$, it

follows that $k_{het} \approx 4\pi r_0^2 k_s c_0 = 4\pi \left(\frac{3m}{4\pi N \rho} \right)^{2/3} k_s c_0$ is effectively constant since k_s is tiny and m/N is fixed for monodisperse particle distributions. Note that these relationships assume that the particle size remains constant throughout the impurity removal process, since it is assumed that only the impurity dissolves. This distinguishes these expressions from those developed for the surface-controlled, complete dissolution of both liquid[S39] and solid[S40] microparticles discussed in the published literature.

ESI10: ESI References and Notes

S1. See, for example, (a) T. Crook, The origin of limestones, *Nature*, 1924, **114**, 733; (b) W. G. Moore, *A Dictionary of Geography*, 3rd edn., Penguin Books, Harmondsworth, Middlesex, 1963

S2. See, for example, M. Rogerson, H. M. Pedley, J. D. Wadhawan, R. Middleton, New insight into biological influence on the geochemistry of freshwater carbonate deposits, *Geochim. Cosmochim. Acta*, 2008, **72**, 4976.

S3. See, for example, D. L. Holmes, *Elements of Physical Geology*, Thomas Nelson and Sons, London, 1969.

S4. See, for example, M. J. Bradshaw, *A New Geology*, Hodder and Stoughton, London, 1973.

S5. J. M. Hancock, The petrology of the Chalk, *Proc. Geol. Ass.*, 1975, **86**, 499.

S6. D. J. Harrison, F. M. McEvoy, P. J. Henney, D. G. Cameron, E. J. Steadman, S. F. Hobbs, N. A. Spenser, D. J. Evans, G. K. Lott, E. M. Bartlett, M. H. Shaw, D. E. Highley, T. B. Colman, *Mineral Resource Information in Support of National, Regional and Local Planning – Humberside (comprising East Riding of Yorkshire, North Lincolnshire, North-East Lincolnshire and City of Kingston-upon-Hull*, British Geological Survey Commissioned Report CR/04/227N, British Geological Survey, Keyworth, 2005.

S7. (a) G. D. Gaunt, T. P. Fletcher, C. J. Wood, *Geology of the Country Around Kingston-upon-Hull and Brigg: Memoir for 1:50000 geological sheets 80 and 89 (England and Wales)*, British Geological Survey, Her Majesty's Stationary Office, London, 1992; (b) F. Whitham, The geology of the Melton Ross chalk quarries, *Humber Geologist*, No. 12, Hull Geological Society, Kingston-upon-Hull, 1999, available online: http://www.hullgeolsoc.co.uk/meltonrs.htm (accessed December 28, 2021).

S8. J. M. Hancock, M. Price, Real chalk balances the water supply, *J. Wine Res.*, 1990, **1**, 45.

S9. M. G. Sumbler, *The Statigraphy of the Chalk Group in Yorkshire and Lincolnshire*, British Geological Survey Technical Report, WA/99/02, British Geological Survey, Keyworth, 1999.

S10. R. N. Mortimore, *Logging the Chalk*, Whittles Publishing, Dunbeath, Caithness, 2014.

S11. C. J. Wood, E. G. Smith, Lithostratigraphical classification of the Chalk in North Yorkshire, Humberside and Lincolnshire, *Proc. Yorks. Geol. Soc.*, 1978, **42**, 263.

S12. J. I. Pitman, Groundwater geochemistry and mass transfer in the East Yorkshire Chalk, in J. C. Crips, F. G. Bell, M. G. Culshaw (eds.), *Groundwater in Engineering Geology*, Geological Society Engineering Geology Special Publication No. 3, Geological Society, London, 1986, p. 177.

S13. A. C. Fowler, X. Yang, Pressure solution and viscous compaction in sedimentary basins, *J. Geophys. Res.*, 1999, **104**, 12989.

S14. C. V. Jeans, D. Long, X.-F. Hu, R. N. Mortimore, Regional hardening of Upper Cretaceous Chalk in eastern England, UK: trace element and stable isotope patterns in the Upper Cenomanian and Turonian Chalk and their significance, *Acta Geol. Polon.*, 2014, **64**, 419.

S15. S. F. Mitchell, The Chalk group (Upper Cretaceous) of the Northern Province, eastern England – a review, *Proc. Yorks. Geol. Soc.*, 2019, **62**, 153.

S16. P. L. Smedley, I. Neumann, R. Farrell, *Baseline Report Series 10: The Chalk Aquifer of Yorkshire and North Humberside*, British Geological Survey Commissioned Report No. CR/04/128, British Geological Survey, Keyworth, 2004.

S17. P. Kent, *Eastern England: From the Tees to The Wash*, 2nd edn., British Regional Geography series for the Institute of Geological Sciences, Her Majesty's Stationary Office, London, 1980.

S18. I. N. Gale, H. K. Rutter, *The Chalk Aquifer of Yorkshire*, British Geological Survey Research Report RR/06/04, British Geological Survey, Keyworth, 2006.

S19. (a) Department of the Environment, *Appraisal of High-Purity Limestones in England and Wales: A Study of Resources, Needs, Uses and Demands: Summary Report*, Department of the Environment, London, 1990; (b) D. J. Harrison, J. M. Hudson, B. Cannell, *Appraisal of High-Purity Limestones in England and Wales: A Study of Resources, Needs, Uses and Demands: Part 1: Resources*, British Geological Survey Mineral Resources Series WF/90/10, British Geological Survey, Keyworth, 1991; (c) D. J. Harrison, High-purity limestones in England and Wales, *Quart. J. Eng. Geol.*, 1993, **26**, 293; (d) D. J. Harrison, D. Highley, A. Bloodworth, R. Bate, D. Cameron, P. Lusty, D. Rayner, *Limestone*, Mineral Planning Factsheet prepared for the Office of the Deputy Prime Minister, British Geological Survey, Keyworth, 2006, available to download from http://www.mineralsUK.com (accessed December 28, 2021); (e) C. Mitchell, High-purity limestone quest, *Industrial Minerals*, 2011, 48.

S20. (a) D. J. Harrison, *The Limestone and Dolomite Resources of the Country Around Buxton, Derbyshire: Description of 1:25000 sheet SK 07 and parts of SK 06 and 08*, Mineral Assessment Report 77 for the Institute of Geological Sciences, Her Majesty's Stationary Office, London, 1981; (b) D. J. Harrison, K. A. McL. Adlam, *Limestones of the Peak: A Guide to the Limestone and Dolomite Resources of the Peak District of Derbyshire and Staffordshire: Description of parts of 1:50000 geological sheets 99, 111, 112, 124 and 125*, Mineral Assessment Report 144 for the British Geological Survey, Her Majesty's Stationary Office, London, 1985.

S21. See, for example, D. K. Todd, L. W. Mays, *Groundwater Hydrology*, 3rd edn., Wiley, New Delhi, 2005.
S22. M. Whitfield, Thermodynamic limitations on the use of the platinum electrode in E_h measurements, *Limnol. Oceanogr.*, 1974, **19**, 857.
S23. P. Shand, W. M. Edmunds, A. R. Lawrence, P. L. Smedley, S. Burke, *The Natural (Baseline) Quality of Groundwater in England and Wales*, Environment Agency Technical Report NC/99/74/24, Groundwater Programme Research Report RR/07/06, British Geological Survey, Keyworth, 2007.
S24. D. R. Champ, J. Gulens, R. E. Jackson, Oxidation-reduction sequences in groundwater flow systems, *Can. J. Earth Sci.*, 1979, **16**, 12.
S25. P. L. Smedley, B. R. Gibbs, J. M. Trafford, *National Groundwater Survey: Chalk Aquifer Study – Hydrogeochemistry and Water Quality of the Chalk Aquifer of North Humberside and Yorkshire*, Hydrology Series Technical Report WD/96/80C, British Geological Survey, Keyworth, 1996.
S26. W. M. Edmunds, W. G. Darling, D. G. Kinniburgh, L. Dever, P. Vachier, *Chalk Groundwater in England and France: Hydrogeochemistry and Water Quality*, British Geological Survey Research Report SD/92/2, Keyworth, 1992.
S27. K. van Balen, Understanding the lime cycle and its influence on historical construction practice, in S. Huerta, I. Juan de Herrera, A. E. Benvenuto, F. Dragados (eds.), *Proceedings of the First International Congress on Construction History*, Madrid, January 20-24, 2003.
S28. See, for example, S. G. Simpson, The effect of the presence of filter paper on permanganate-oxalate titrations, *J. Ind. Eng. Chem.*, 1921, **13**, 1152
S29. The blue pentavalent manganese ion hypomanganate has only ever been observed in strongly alkaline solutions, where it is known to be unstable. See, for example, the electrochemical generation of hypomanganate: (a) H. H. Miller, L. B. Rogers, Pentavalent manganese, *Science*, 1949, **109**, 61; or its generation through reaction with sulfite to yield MnO_2: (b) L. I. Simandi, M. Jaky, Z. A. Schelly, Short-lived manganate(VI) and manganate(V) intermediates in the permanganate oxidation of sulfite ion, *J. Am. Chem. Soc.*, 1984, **106**, 6866. The characteristic blue colour is discussed in (c): L. E. Orgel, The visible spectrum of the hypomanganate ion, *Molec. Phys.* 1964, **7**, 397.
S30. See, for example, G. T. Austin, Shreve's Chemical Process Industries, fifth ed., McGraw-Hill, New York, USA, 1984.
S31. S. Gates-Rector, T. Blanton, The powder diffraction file: a quality materials characterization database. *Powder Diffraction*, 2019, **34**, 352.
S32. L. B. McCusker, R. B. von Dreele, D. E. Cox, D. Louer, P. Scardi, Rietveld refinement guidelines, *J. Appl. Cryst.* 1999, **32**, 36.
S33. M. A. G. Aranda, A. G. De la Torre, L. León-Reina, Powder diffraction characterisation of cements, in C. J. Gilmore, J. A. Kaduk, H. Schenk (eds.), *International Tables for Crystallography*, volume H, chapter 7.12, Wiley, Chichester, 2019, p. 856
S34. (a) S. Licht, V. Naschitz, L. Halperin, L. Lin, J. Chen, S. Ghosh, B. Liu, Analysis of ferrate(VI) compounds and super-iron Fe(VI) battery cathodes: FTIR, ICP, titimetric, XRD, UV/VIS, and electrochemical characterisation, *J. Power Sources*, 2001, **101**, 167; (b) Y. L. Wang, S. H. Ye, J. K. Bo, Y. Y. Wang, F. Wu, Electrochemical reduction mechanism of Fe(VI) at a porus Pt black electrode, *J. Electrochem. Soc.*, 2009, **156**, A572; (c) S. Barışçı, F. Ulu, H. Särkkä, A. Dimoglo, M. Sillanpää, Electrosynthesis of ferrate(VI) ion using high purity iron electrodes: optimisation of influencing parameters on the process and investigating its stability, *Int. J. Electrochem. Sci.*, 2014, **9**, 3099; (d) Y.-L. Wei, Y.-S. Wang, C.-H. Liu, Preparation of potassium ferrate from spent steel pickling liquid, *Metals*, 2015, **5**, 1770; (e) J.-Q. Jiang, C. Stanford, M. Petri, Practical application of ferrate(VI) for water and wastewater treatment – site study approach, *Water-Energy Nexus*, 2018, **1**, 42; (f) B. Shao, H. Dong, X. Guan, Role of ferrate(IV) and ferrate(V) in activating ferrate(VI) by calcium sulphite for enhanced oxidation of organic contaminants, *Environ. Sci. Technol.*, 2019, **53**, 894; (g) P. C. W. Cheung, D. R. Williams, J. Barrett, J. Barker, D. W. Kirk, On the origins of some spectroscopic properties of "purple iron" (the tetroxoferrate(VI) ion and its Pourbaix safe-space, *Molecules*, 2021, **26**, 5266.
S35. D. R. Lide (ed.), *CRC Handbook of Chemistry and Physics*, 76th edn., CRC Press, Boca Raton, Fl., 1995.
S36. See, for example, (a) H. P. Hopkins, Jr., C. A. Wulff, The solution thermochemistry of polyvalent electrolytes: I: calcium hydroxide, *J. Phys. Chem.*, 1965, **69**, 6; (b) W. B. Euler, L. J. Kirschenbaum, B. Ruekberg, Determination of K_{sp}, ΔG^0, ΔH^0 and ΔS^0, *J. Chem. Educ.*, 2000, **77**, 1039.
S37. (a) J. Wang, T. C. Keener, G. Li, S.-J. Khang, The dissolution rate of $Ca(OH)_2$ in aqueous solutions, *Chem. Eng. Commun.*, 1998, **169**, 167; (b) S. Kilic, G. Toprak, E. Ozdemir, Stability of $CaCO_3$ in $Ca(OH)_2$ solution, *Int. J. Mineral Process.*, 2016, **147**, 1.
S38. (a) J. F. Zimmerman, Diffusion and activation control in heterogeneous reactions, *J. Phys. Chem.*, 1949, **53**, 562; (b) L.L. Bircumshaw, A. C. Riddiford, Transport control in heterogeneous reactions, *Q. Rev. Chem. Soc.*, 1952, **6**, 157; (c) J. H. Atherton, Mechanism in two-phase reaction systems: coupled mass transfer and chemical reaction, in R. G. Compton,

G. Hancock (eds.), *Research in Chemical Kinetics*, volume 2, Elsevier, Amsterdam, 1994, p.193.

S39. (a) J. D. Wadhawan, R. G. Evans, C. E. Banks, S. J. Wilkins, R. R. France, N. J. Oldham, A. J. Fairbanks, B. Wood, D. J. Walton, U. Schröder, R. G. Compton, Voltammetry of electroactive oil droplets: electrochemically induced ion insertion, expulsion and reaction processes at microdroplets of *N*,*N*,*N'*,*N'*-tetraalkyl-*para*-phenylenediamines (TRPD, R = *n*-butyl, *n*-hexyl, *n*-heptyl and *n*-nonyl), *J. Phys. Chem. B*, 2002, **106**, 9619; (b) J. D. Wadhawan, R. G. Evans, R. G. Compton, Voltammetric characteristics of graphite electrodes modified with microdroplets of *n*-butylferrocene, *J. Electroanal. Chem.*, 2002, **533**, 71; (c) J. D. Wadhawan, A. J. Wain, A. N. Kirkham, D. J. Walton, B. Wood, R. R. France, S. D. Bull, R. G. Compton, Electrocatalytic reactions mediated by *N*,*N*,*N'*,*N'*-tetraalkyl-1,4-phenylenediamine redox liquid microdroplet-modified electrodes: chemical and photochemical reactions in, and at the surface of, femtolitre droplets, *J. Am. Chem. Soc.*, 2003, **125**, 11418.

S40. (a) M. G. Segal, R. M. Sellers, Reactions of solid iron(III) oxides with aqueous reducing agents, *J. Chem. Soc.*, *Chem. Commun.*, 1980, 991; (b) M. G. Segal, R. M. Sellers, Kinetics of metal oxide dissolution: reductive dissolution of nickel ferrite by tris(picolinato)vanadium(II), *J. Chem. Soc., Faraday Trans. I*, 1982, **78**, 1149; (c) A. Mills, H. L. Davies, M. S. Garley, Kineticsnfor the surface-controlled dissolution of a powder dispersion with a log-Normal distribution in particle size, *J. Chem. Soc.*, *Faraday Trans.*, 1990, **86**, 2163; (d) A. Mills, D. Worsley, Kinetics of redox dissolution of soft-centre particles, *J. Chem. Soc.*, *Faraday Trans.*, 1990, **86**, 3405; (e) A. Mills, P. Sawunyama, Oxidative dissolution of ruthenium dioxide hydrate by periodate ions, *J. Chem. Soc.*, *Faraday Trans.*, 1992, **88**, 2487; (f) C. L. Forryan, O. V. Klymenko, C. M. Brennan, R. G. Compton, Reactions at the solid-liquid interface: surface-controlled dissolution of solid particles: the dissolution of potassium bicarbonate in dimethylformamide, *J. Phys. Chem. B*, 2005, **109**, 2862; (g) C. L. Forryan, O. V. Klymenko, C. M. Brennan, R. G. Compton, Heterogeneous kinetics of the dissolution of an inorganic salt, potassium carbonate, in an organic solvent, dimethylformamide, *J. Phys. Chem. B*, 2005, **109**, 8263; (h) C. L. Forryan, O. V. Klymenko, S. J. Wilkins, C. M. Brennan, R. G. Compton, Experimental and theoretical study of the surface-controlled dissolution of cylindrical particles: application to solubilisation of potassium hydrogen carbonate in hot dimethylformamide, *J. Phys. Chem. B*, 2005, **109**, 20786; (i) C. L. Forryan, R. G. Compton, O. V. Klymenko, C. M. Brennan, C. L. Taylor, M. Lennon, Comparative solubilisation of potassium carbonate, sodium bicarbonate and sodium carbonate in hot dimethylformamide: application of cylindrical particle surface-controlled dissolution theory, *Phys. Chem. Chem. Phys.*, 2006, **8**, 633.